PHYSICAL REVIEW B **78**, 115415 (2008)

Direct generation of terahertz surface plasmon polaritons on a wire using electron bunches

P. W. Smorenburg, W. P. E. M. Op 't Root, and O. J. Luiten
Eindhoven University of Technology, Coherence and Quantum Technology, P.O. Box 513, 5600 MB Eindhoven, The Netherlands
(Received 20 May 2008; revised manuscript received 19 August 2008; published 16 September 2008)

We propose to generate terahertz surface plasmon polaritons (SPPs) on a metal wire by launching electron bunches onto a tapered end of the wire. To show the potential of this method, we solve Maxwell's equations for the appropriate boundary conditions. The metal wire tip is modeled by a perfectly conducting semi-infinite cone. It is shown that the SPPs can be recovered from the idealized fields by well-known perturbation techniques. The emitted radiation is strongly concentrated into a narrow solid angle near the cone boundary for cones with a small opening angle. We calculate that, using currently available technology, subpicosecond SPPs with peak electric fields of the order of MV/cm on a 1 mm diameter wire can be obtained.

DOI: 10.1103/PhysRevB.78.115415 PACS number(s): 73.20.Mf, 41.60.Dk

I. INTRODUCTION

Terahertz surface plasmon polaritons (SPPs) on a metal wire recently received a lot of attention.[1–10] It has been shown that these SPPs can efficiently be focused below the diffraction limit by periodically corrugating the wire[7,8] or tapering the wire into a tip.[9] This leads to electromagnetic (e.m.) terahertz pulses that are both very strong and highly localized, making it possible to study materials at terahertz frequencies with subwavelength spatial resolutions.[11,12] Applications include near-field optical microscopy,[13,14] imaging of semiconductor structures[15,16] or biological tissues,[17,18] single-particle sensing,[19,20] and terahertz spectroscopy.[21,22]

Another benefit of the wire geometry is that it acts as an efficient waveguide for terahertz SPPs. Recently it has been shown that terahertz SPPs can propagate along a wire over long distances with low attenuation and dispersion.[1–5] This enables endoscopic delivery of terahertz radiation to samples in applications where line of sight access is not available.[1] Several other structures have been proposed as waveguides for terahertz SPPs, including coaxial lines,[23] metal tubes,[24] and nonmetallic guides.[25,26] However, the feasibility of these guides is limited by either high attenuation or high dispersion. An exception is the parallel-plate waveguide,[27] but in this case the large cross-sectional area may be a problem for many terahertz applications.

Despite the promising properties of terahertz SPPs guided by a metal wire, it has proven difficult to efficiently generate SPPs of appreciable amplitude. In contrast, over the last years, several sources have become available that generate intense *free-space* terahertz radiation pulses with broad bandwidth and peak electric fields that approach the MV/cm regime. Technologies of the latter include accelerator-based sources generating coherent radiation[28–30] and table-top systems producing radiation by optical rectification of femtosecond laser pulses.[31] However, up to now, efficient coupling of these free-space terahertz pulses into the guided mode on a wire has been difficult. Currently, terahertz SPPs are generated by scattering the linearly polarized free-space waves into a radially polarized wave, which is then coupled onto the wire.[1] However, due to the poor spatial overlap between the free-space radiation wave form and the SPP wave form, the coupling efficiency is very low (typically less than 1%[32]). Hence the attainable SPP electric-field strength is limited to the kV/cm range by current methods. A proposed method to overcome this low coupling efficiency is to create radially polarized terahertz radiation using a radially symmetric photoconductive antenna.[32]

In this paper, we propose a method to generate terahertz SPPs on a wire *directly*, that is, without the creation of free-space terahertz radiation as an intermediate step. Similar to the method proposed in Ref. 32, in our method the guided mode on the wire is excited by a radially polarized field, thereby avoiding the poor coupling efficiency described above. We propose to generate terahertz SPPs by launching electron bunches onto a metal wire, which is tapered into a conical tip, as is illustrated in Fig. 1. When passing the conical vacuum-metal boundary, the bunch will generate a radially polarized coherent transition radiation (CTR) field, of which terahertz SPPs along the boundary are part. These excited SPPs will propagate onto the wire subsequently. We calculate that, with currently available electron bunches, subpicosecond SPPs with peak electric fields of the order of MV/cm could be created on a 1-mm diameter metal wire.

Transition radiation is generated when an electron passes a vacuum-metal boundary,[33–35] and the radiation is radially polarized due to the radial polarization of the Coulomb field of the electron.[36] The radiated energy from a single electron is very small. However, when N electrons pass the boundary and radiate coherently, they produce N^2 as much energy as a single electron. In the latter case, the radiated energy can be considerable. Because the radiation profile and spectrum depend on the bunch form, CTR is a well-known diagnostic tool to characterize the spatial distribution of electron bunches.[37–41] Note that in this paper we use the term "coherence" as it is commonly used in classical electromagnetism, that is, referring to the constructive interference of the electromagnetic field contributions from different parts of the source. Such coherent field addition takes place if the electrons are compressed into a bunch of dimensions less than the wavelength, which means that bunches of size ~ 300 μm radiate coherently at frequencies up to about 1 THz. Recently, such generation of intense free-space terahertz radiation by CTR emitted at a planar interface has been demonstrated, using linac[42] or laser-wakefield[43] accelerated bunches and resulting in electric fields of the order of MV/cm after focusing of the radiation.

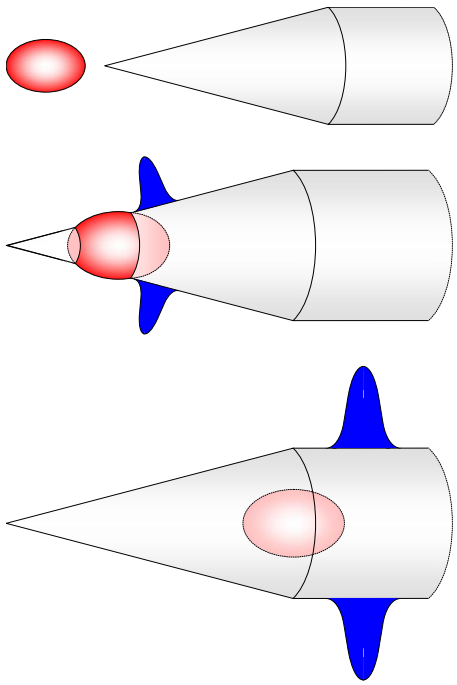

FIG. 1. (Color online) Principle of terahertz SPP (blue bell-shaped pulse) generation on a wire by launching electron bunches (red oval) onto a conical tip.

We propose to generate terahertz SPPs directly by launching electron bunches onto a tapered wire tip instead of coupling free-space CTR emitted at a planar interface onto a metal wire. This has two benefits: first, electrons are capable of exiting SPPs directly, in contrast to photons where an additional coupling medium is necessary to match the wave vectors of the photons and SPPs. Second, for sharp tips the electrons pass the vacuum-metal boundary at grazing incidence, which enhances the transition radiation due to an increased radiation formation length.[44]

It is well known that the radiated power of transition radiation is proportional to $\log \gamma$,[33] where $\gamma=(1-\beta^2)^{-1/2}$ is the relativistic factor of the electron bunch. Therefore, in principle there is no need to accelerate the bunch to high energies; typically $\gamma=5-10$, i.e., an electron energy of 2–5 MeV, is sufficient for transition radiation methods. Furthermore, it has been shown previously that mildly relativistic bunches of the required size can be made using a table-top setup.[45–48] Thus, a technological benefit of our method is that it can be applied using an overall table-top system.

In this paper we calculate analytically what terahertz SPP electric fields can be obtained by launching electron bunches onto a tapered metal tip. Hence a considerable part of this paper will be devoted to an analytical calculation of the transition radiation that is produced by the bunch impinging on the conical tip in Fig. 1. This calculation amounts to finding a solution of Maxwell's equations for the electric field. This field should be consistent with the presence of the electron bunch and should satisfy appropriate boundary conditions at the metal surface. However, fully solving Maxwell's equations for a conical geometry is notoriously difficult. The problem is greatly simplified by assuming that the metal is an ideal conductor so that the electric field is perpendicular to the metal surface outside the tip and is zero inside the tip. In making this assumption, however, one inherently neglects the possibility of the existence of SPPs. Nevertheless, for good conductors, the SPPs can be recovered from the idealized field by well-known perturbation techniques. This is the approach followed in this paper. Furthermore, since we are only interested in the SPPs that result at distances from the tip that are large compared to the wavelength, we have applied far-field approximations, which greatly simplify the calculations.

The remainder of this paper is organized as follows: In Sec. II, it is shown how the SPP field may be obtained from the idealized field. Having this connection established, we proceed to calculate the transition radiation field of a point charge impinging on an ideally conducting conical tip in Sec. III. In Sec. IV the results of this calculation are presented for a number of concrete cases for the opening angle of the tip. It will be shown that for sharp tips the transition radiation strongly concentrates into a narrow bundle grazing the tip surface, leading to very intense SPP fields. In Sec. V it is shown that the calculated field expressions exactly agree with closed analytical expressions obtained by different methods for the limiting cases of a tip with a very large opening angle (that is, a planar surface) and that of a tip with a very small opening angle (that is, a semi-infinite line). The results for the single point charge are then extended to the case of electron bunches in Sec. VI. This allows calculation of the SPP field that can be readily obtained in practical applications, which is shown in Sec. VII. Section VIII summarizes the conclusions of this paper.

A note on the notation: nearly all quantities in this paper are expressed in Fourier transformed form according to $X \equiv X(\omega) \equiv (2\pi)^{-1/2}\int_{-\infty}^{\infty} X(t)e^{i\omega t}dt$. Time-domain quantities will be denoted explicitly like $X(t)$.

II. SPPs AS PERTURBATION OF RADIATION FIELD AT IDEAL CONDUCTOR

Considered throughout the paper is a semi-infinite metal cone with an opening angle of 2δ placed along the negative z axis of a spherical coordinate system and a charge q moving along the positive z axis toward the cone tip, as shown in Fig. 2. Suppose that, using the idealization that the metal is a perfect conductor, the magnetic field can be calculated analytically for every point P outside the cone. In the case of a good but not perfect conductor this idealized field can be extended into the conductor by approximate methods. This is common practice in resonant cavity and waveguide design and yields the well-known skin field,[49]

$$\boldsymbol{E}_{\text{skin}} \approx (1-i)\sqrt{\frac{\omega}{2\mu\sigma}}e^{(1-i)\frac{\xi}{\Delta}}(\boldsymbol{n}\times\boldsymbol{B}_{\parallel}), \tag{1}$$

with

$$\Delta = \sqrt{\frac{2}{\mu\omega\sigma}} \tag{2}$$

as the skin depth. Here, $\boldsymbol{B}_{\parallel}$ is the idealized magnetic field at the surface (which is parallel to the surface). Furthermore, $\boldsymbol{n}$

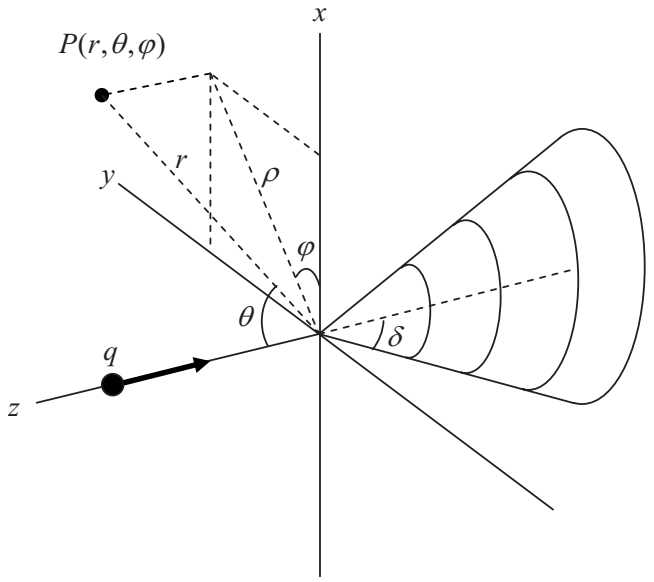

FIG. 2. Definition of coordinates.

denotes the outward normal vector at the metal surface and ξ a coordinate along this vector, μ denotes the permeability, and σ denotes the conductivity of the metal. As is typical for good conductors, the skin field decreases exponentially with the depth $-\xi$ into the metal. In the following sections, the idealized fields are calculated from which the skin field [Eq. (1)] can be determined for every point on the cone surface. This skin field and the accompanying magnetic field can be seen as electromagnetic disturbances in the metal skin with a forced distribution $\boldsymbol{B}_{\|}(r,\pi-\delta,\phi)$. They will propagate independently as SPPs along the cone surface and onto a wire only if their wave form matches that of the SPPs, that is, if the field [Eq. (1)] is matched with freely propagating surface waves. To see whether this is true, the electric SPP field $\boldsymbol{E}_{\mathrm{SPP}}$ on a nonideal cone has to be calculated and compared to the skin field [Eq. (1)].

The field $\boldsymbol{E}_{\mathrm{SPP}}$ is a solution of the homogeneous Helmholtz equation,

$$(\nabla^2 + k^2)\boldsymbol{E}_{\mathrm{SPP}} = 0, \tag{3}$$

with boundary conditions appropriate to the conical geometry of Fig. 2. Unfortunately, no closed-form solutions exist for this. However, the eikonal or WKB approximation may be used to approximate $\boldsymbol{E}_{\mathrm{SPP}}$ for small opening angle cones.[9] This is shown in Appendix A. Applying the Drude model[50] for the permittivity of the metallic cone, the result is that

$$\boldsymbol{E}_{\mathrm{SPP}} \approx (1-i)\sqrt{\frac{\omega}{2\mu\sigma}}e^{(1-i)\frac{\rho-|z|\tan\delta}{\Delta}}B_0 e^{ik_z z}\boldsymbol{e}_z \tag{4}$$

is an approximate solution of Eq. (3) provided that

$$k|z| \gg 1, \tag{5}$$

$$\frac{|z|\tan\delta}{\Delta} \gg 1, \tag{6}$$

$$\left|\frac{d}{da}\frac{1}{k_z(a)}\right|\tan\delta \ll 1. \tag{7}$$

In Eq. (4), B_0 is an amplitude with units of magnetic field. In Eq. (7), $k_z(a)$ denotes the propagation constant of SPPs along a cylinder with radius a, which is discussed in Appendix A. Comparison of Eqs. (1) and (4) shows that the skin field obtained from a calculation of the idealized field outside the cone is of the same form as the field of freely propagating SPPs, identifying the amplitude B_0 with $|\boldsymbol{B}_{\|}|$ and noting that $\boldsymbol{B}_{\|}$ is polarized in the ϕ direction. The latter is the property of the transition radiation field that we exploit using the cone geometry.

Therefore, we can conclude that the amplitude of the transition radiation field at the cone surface, calculated under the assumption of an ideally conducting cone, can be identified with the amplitude of the excited SPPs as long as conditions (5)–(7) apply. Thus we proceed by calculating the idealized field in the next sections, returning to the SPP field in Sec. VII.

III. RADIATION FIELD CALCULATION

A. Dyadic Green's function

To calculate the electric radiation field generated by the moving point charge in Fig. 2, we use a dyadic Green's-function method. Dyadic Green's functions are an important tool in electromagnetic theory[51,52] and are often used to calculate how incoming electromagnetic radiation is scattered by some given body.[53] In contrast, the incoming field considered here is that of a moving physical charge. In particular, the field propagates in the negative z direction with a speed less than that of light.

Considering the idealized situation of a perfectly conducting cone embedded in vacuum, the total electric field outside the cone satisfies the inhomogeneous Helmholtz equation,

$$(\nabla^2 + k^2)\boldsymbol{E} = \epsilon_0^{-1}\nabla\rho - i\omega\mu_0\boldsymbol{J},$$

$$0 \le \theta < \pi - \delta, \tag{8}$$

where ρ is the charge density, $\boldsymbol{J}$ is the current density, and ϵ_0 and μ_0 are the permittivity and permeability of vacuum, respectively. At the cone, the field is subject to the boundary condition,

$$\boldsymbol{n}\times\boldsymbol{E} = \boldsymbol{0}, \quad \theta = \pi - \delta. \tag{9}$$

Furthermore, we are interested in the far-field part of the electric field, that is, in that component, which represents electromagnetic radiation. This component $\boldsymbol{E}_T$ is the transverse part[49] of the vector field $\boldsymbol{E}$ such that

$$\nabla\cdot\boldsymbol{E}_T = 0. \tag{10}$$

As is known, while applying a Green's-function method one first calculates the field response at some position $\boldsymbol{r}$ due to a unit point source at another position $\boldsymbol{r}_0$, and then integrates the result over the full source distribution to obtain the full field. More exactly, the method is as follows:[51] Suppose that a dyadic (i.e., nine component) function $\mathfrak{G}$ of two coor-

dinate vectors $\boldsymbol{r}$ and $\boldsymbol{r}_0$ can be found, such that

$$(\nabla^2 + k^2)\mathfrak{G}(\boldsymbol{r},\boldsymbol{r}_0) = \mathfrak{I}\delta^3(\boldsymbol{r}-\boldsymbol{r}_0),$$

$$0 \le \theta < \pi - \delta, \tag{11}$$

where $\mathfrak{I}$ is the identity dyadic or idemfactor and δ^3 is the three-dimensional Dirac delta function. Suppose further that, at the cone, $\mathfrak{G}$ satisfies the boundary condition

$$\boldsymbol{n} \times \mathfrak{G} = \mathfrak{O}, \quad \theta = \pi - \delta, \tag{12}$$

with $\mathfrak{O}$ as the zero dyadic. Then it can be shown that the transverse part of the electric field that satisfies Eqs. (8) and (9) is given by

$$\boldsymbol{E}_T(\boldsymbol{r}) = -i\omega\mu_0 \int\int\int_{V_0} \mathfrak{G}_T(\boldsymbol{r},\boldsymbol{r}_0)\cdot\boldsymbol{J}(\boldsymbol{r}_0)dV_0, \tag{13}$$

where V_0 is the entire space outside the cone. Here, the dyadic $\mathfrak{G}_T$ is the transverse part of $\mathfrak{G}$,[51] i.e., the part of $\mathfrak{G}$ for which

$$\nabla\cdot\mathfrak{G}_T = \boldsymbol{0}. \tag{14}$$

Equation (13) can be derived by manipulation of Eqs. (8)–(12) and depends on the vanishing of several surface integrals. This is shown in Appendix B. Note in particular the well-known result that the far-field only depends on the current density and not on the charge density.

With Eq. (13), the problem of finding the radiation field generated by the point charge in Fig. 2 is reduced to evaluation of the dyadic Green's function $\mathfrak{G}_T$, current density $\boldsymbol{J}$, and a three-dimensional integral. The time-domain and Fourier transformed current densities of a point charge that moves along the z axis in the negative direction with velocity βc and passes the origin at time $t=0$, are given in Cartesian coordinates by

$$\boldsymbol{J}(t) = -q\beta c\,\delta(x)\,\delta(y)\,\delta(z+\beta ct)\boldsymbol{e}_z, \quad t<0, \tag{15}$$

$$\boldsymbol{J}(\omega) = -(2\pi)^{-1/2} q\,\delta(x)\,\delta(y)e^{-i\frac{k}{\beta}z}\boldsymbol{e}_z, \quad z>0. \tag{16}$$

Thus, in the Fourier domain the current takes the form of a line distribution along the positive z axis. The dyadic Green's function $\mathfrak{G}$ of course depends on the geometry of the volume V_0, that is, on the angle δ. Several representations for $\mathfrak{G}$ are known, one of which takes the form of an expansion in terms of dyadic products of the eigenfunctions of the vectorial Helmholtz equation.[51,52] This expansion is shown in full in Appendix C. Taking the transverse part $\mathfrak{G}_T$ of this representation and keeping only terms that yield a nonzero contribution to the integral in Eq. (13), reduces the Green's function to a simpler form. This is shown in Appendix C. The result is

$$\mathfrak{G}_T = -ik\sum_\sigma \frac{\alpha_\sigma^2}{\sigma(\sigma+1)} \begin{cases} \boldsymbol{N}_\sigma^{(1)}(\boldsymbol{r})\boldsymbol{N}_\sigma^{(3)}(\boldsymbol{r}_0) & r<r_0 \\ \boldsymbol{N}_\sigma^{(1)}(\boldsymbol{r}_0)\boldsymbol{N}_\sigma^{(3)}(\boldsymbol{r}) & r>r_0 \end{cases}, \tag{17}$$

where the eigenvalues $\{\sigma\}$ are the solutions of Eq. (C12), α_σ and $\boldsymbol{N}_\sigma$ are given by Eqs. (C7) and (C11), respectively, and subscripts $m=0$ have been omitted.

B. Field quantities in the far zone

Substitution of current (16) and Green's function (17) in Eq. (13) yields an expression for the transverse electric field generated by the moving point charge. As is shown in Appendix D, in the far zone $kr\to\infty$ this expression reduces to

$$\boldsymbol{E}_T \approx \frac{\mu_0\omega q}{\sqrt{2\pi}}\frac{e^{ikr}}{kr}\sum_\sigma \alpha_\sigma^2 e^{-i\sigma\frac{\pi}{2}} I_\sigma(\beta) P_\sigma^1(\cos\theta)\boldsymbol{e}_\theta, \tag{18}$$

with

$$I_\sigma(\beta) \equiv \frac{\sqrt{\pi}\Gamma(\sigma)}{2\Gamma\left(\sigma+\frac{3}{2}\right)} e^{-i\sigma\frac{\pi}{2}} \cdot \left(\frac{\beta}{2}\right)^\sigma {}_2F_1\left(\frac{\sigma}{2},\frac{\sigma+1}{2};\sigma+\frac{3}{2};\beta^2\right). \tag{19}$$

Here, Γ denotes the Gamma function and ${}_2F_1$ is the hypergeometric function. The curl of the electric field yields the magnetic field in the far zone,

$$\boldsymbol{B} = \frac{1}{i\omega}\nabla\times\boldsymbol{E}_T \approx \frac{\mu k q}{\sqrt{2\pi}}\sum_\sigma \alpha_\sigma^2 e^{-i\sigma\frac{\pi}{2}} I_\sigma(\beta) P_\sigma^1(\cos\theta)\frac{e^{ikr}}{kr}\boldsymbol{e}_\phi. \tag{20}$$

The (time integrated) energy flow per unit of surface area per unit of frequency is given by the spectral Poynting vector,[36]

$$\boldsymbol{S}(\omega) = \frac{2}{\mu}\mathrm{Re}[\boldsymbol{E}_T(\omega)\times\boldsymbol{B}^*(\omega)], \tag{21}$$

here defined such that $\boldsymbol{a}\cdot\int_0^\infty \boldsymbol{S}(\omega)d\omega$ gives the energy flow per unit of area in the direction of a unit vector $\boldsymbol{a}$. The spectral brightness, defined as the energy flow W per unit of frequency ω per unit of solid angle Ω, is

$$\frac{\partial^2 W}{\partial\omega\,\partial\Omega} = r^2\boldsymbol{e}_r\cdot\boldsymbol{S}(\omega), \tag{22}$$

which yields

$$\frac{\partial^2 W}{\partial\omega\,\partial\Omega} = \frac{q^2}{4\pi\epsilon_0 c}\left|\sum_\sigma 2\alpha_\sigma^2 e^{-i\sigma\frac{\pi}{2}} I_\sigma(\beta) P_\sigma^1(\cos\theta)\right|^2. \tag{23}$$

This is the transition radiation generated by the moving point charge in Fig. 2 as it passes from vacuum into the perfectly conducting cone at the cone tip, resolved into the spectral components ω and the observation angle θ. Note that the brightness does not depend on the frequency, which is a characteristic for transition radiation from a point charge.[33] Of course, for a physical metal, the permittivity is frequency dependent so that the brightness quickly decreases as the frequency approaches the metal's plasma frequency. Therefore the total radiated energy $\int\int\frac{\partial^2 W}{\partial\omega\partial\Omega}d\omega d\Omega$ remains finite. However, here we are interested in terahertz frequencies, which are well below typical plasma frequencies.

Finally, to obtain the radiated energy per unit of frequency or spectral intensity, the spectral brightness is integrated over the angular coordinates. This gives

$$\frac{\partial W}{\partial \omega} = \frac{q^2}{4\pi\epsilon_0 c}\sum_{\sigma}\left(4\frac{\alpha_{\sigma 0}^4}{\alpha_{\sigma 1}^2}|I_\sigma|^2 + 8\,\mathrm{Re}\sum_{\tau>\sigma}\alpha_{\tau 0}^2\alpha_{\sigma 0}^2 e^{-i(\tau-\sigma)\frac{\pi}{2}} I_\tau I_\sigma^* p_{\tau,\sigma}\right), \tag{24}$$

with $\alpha_{\sigma 0}$ and $\alpha_{\sigma 1}$ given by Eq. (C7), and with[54]

$$p_{\tau,\sigma} = \frac{2\pi \sin\delta}{\tau(\tau+1)-\sigma(\sigma+1)}\cdot[P_\tau^1(-\cos\delta)P_\sigma^2(-\cos\delta) - P_\sigma^1(-\cos\delta)P_\tau^2(-\cos\delta)],$$

where the asterisk denotes complex conjugation.

C. Spectral brightness in the narrow-angle cone limit

To validate the results of the previous section with alternative analytic methods later on, the behavior of the spectral brightness in the narrow-angle cone limit will be discussed. In order to obtain this behavior, we study the form of the dyadic Green's function [Eq. (17)] in this limit. The Green's function depends on the cone opening angle δ via the set of eigenvalues $\{\sigma\}$, which are the solutions of Eq. (C12). Its angular dependency is described by the Legendre functions in Eq. (C11), and from the previous section it is apparent that only the component,

$$\boldsymbol{e}_{z_0}\cdot\mathfrak{G}_T\cdot\boldsymbol{e}_\theta = -ik\sum_\sigma \alpha_\sigma^2[\boldsymbol{e}_{z_0}\cdot\boldsymbol{N}_\sigma^{(1)}(\boldsymbol{r}_0)][\boldsymbol{e}_\theta\cdot\boldsymbol{N}_\sigma^{(3)}(\boldsymbol{r})] \tag{25}$$

of the Green's function contributes to the spectral brightness [Eq. (23)]. In the following, we show that this expression and therefore the spectral brightness contains two components: one that is well behaved in all directions θ and one that is sharply peaked near narrow-angle cones. In Ref. 55 a series similar to Eq. (25) is studied and the following results are obtained.

As $\delta\to 0$, (the cone approaches a half line), the eigenvalues approach the integers from above, such that

$$\sigma_n = n + \sigma_0, \tag{26}$$

$$\sigma_0 \to \frac{1}{2\ln\frac{2}{\delta}}, \tag{27}$$

as $\delta\to 0$, where $n\in\mathbb{N}$. The terms $\boldsymbol{e}_\theta\cdot\boldsymbol{N}_\sigma^{(3)}(\boldsymbol{r})$ in Eq. (25) contain noninteger degree, first-order Legendre functions. These grow very rapidly near the cone boundary if $\delta\ll 1$ because then the argument $\cos\theta$ approaches the singularity $\lim_{x\to -1} P_\sigma^1(x)=\infty$. The functions may be approximated by

$$P_{n+\sigma_0}^1(\cos\theta) \approx P_n^1(\cos\theta) + (-1)^{n+1}\frac{2\sigma_0}{\sin\theta}, \quad \sigma_0 \ll 1. \tag{28}$$

On the other hand, the terms $\boldsymbol{e}_{z_0}\cdot\boldsymbol{N}_\sigma^{(1)}(\boldsymbol{r}_0)$ in Eq. (25) contain zeroth-order Legendre functions, which are evaluated at $\theta_0=0$. This is because the source current [Eq. (16)] is confined to the z axis where $\boldsymbol{e}_{z_0}=\boldsymbol{e}_{r_0}$. Hence

$$P_{n+\sigma_0}(\cos\theta_0) = P_n(\cos\theta_0) \equiv 1, \tag{29}$$

irrespective of σ_0. Finally, the scale factors α_σ are approximately equal to

$$\alpha_{n+\sigma_0}^2 \approx \alpha_n^2 = \frac{2n+1}{4\pi}. \tag{30}$$

Note that Eq. (28) splits the noninteger degree Legendre functions into a regular term $P_n^1(\cos\theta)$ and an additional term $(-1)^{n+1}2\sigma_0/\sin\theta$. The latter strongly grows near the cone boundary, where $\pi-\theta\ll 1$, but is small otherwise due to the smallness of σ_0. The extent of the angular regime in which the second term is dominant may be characterized by the angle at which this term becomes larger than the regular term. For each $n\geq 1$, this angle is larger than

$$\theta_c = \pi - \sqrt{\frac{1}{\ln\frac{2}{\delta}}}. \tag{31}$$

In Eq. (28), the regular term vanishes altogether for $n=0$ since $P_0^1(x)\equiv 0$, but also in this case Eq. (31) is a convenient measure for the angular extent of the second term since the latter grows larger than unity at this angle.

Substituting Eqs. (26)–(30) in series (25), it is found that the Green's-function component resembles

$$\boldsymbol{e}_{z_0}\cdot\mathfrak{G}_T\cdot\boldsymbol{e}_\theta \approx -ik\sum_{n=1}^{\infty}\alpha_n^2[\boldsymbol{e}_{z_0}\cdot\boldsymbol{N}_n^{(1)}(\boldsymbol{r}_0)][\boldsymbol{e}_\theta\cdot\boldsymbol{N}_n^{(3)}(\boldsymbol{r})] \tag{32}$$

in the regime $0\leq\theta<\theta_c$, while it grows as

$$\boldsymbol{e}_{z_0}\cdot\mathfrak{G}_T\cdot\boldsymbol{e}_\theta \propto \frac{1}{\pi-\theta} \tag{33}$$

in the regime $\theta_c<\theta<\pi-\delta$, that is, close to the cone boundary.

Now, Eq. (32) may be recognized as the dyadic Green's function for free space[51] or rather its component applicable to the problem considered here. Therefore, for a narrow-angle cone and in the regime $0<\theta<\theta_c$, the transition radiation profile [Eq. (23)] resembles the radiation that the point charge in Fig. 2 (which travels along half the z axis and disappears in the origin) would produce *without* the presence of the cone. On the other hand, in the regime $\theta_c<\theta<\pi-\delta$ the electric field is proportional to $(\pi-\theta)^{-1}$ by Eqs. (13) and (33) so that the spectral brightness grows as

$$\frac{\partial^2 W}{\partial\omega\,\partial\Omega} \propto \frac{1}{(\pi-\theta)^2}, \quad \theta_c<\theta<\pi-\delta \tag{34}$$

near the cone boundary. In the very limit that $\delta\to 0$, Eq. (31) yields that $\theta_c\to\pi$. Thus, in this limit, the transition radiation is composed of two contributions: (1) the radiation pattern produced by a point charge moving in free space along half the z axis and (2) an infinitesimally thin and infinitely high radiation peak along the negative z axis.

The latter may be seen as the contribution of a surface wave propagating along the infinitesimally thin cone, which will be shown using an alternative analytic method in Sec. V.

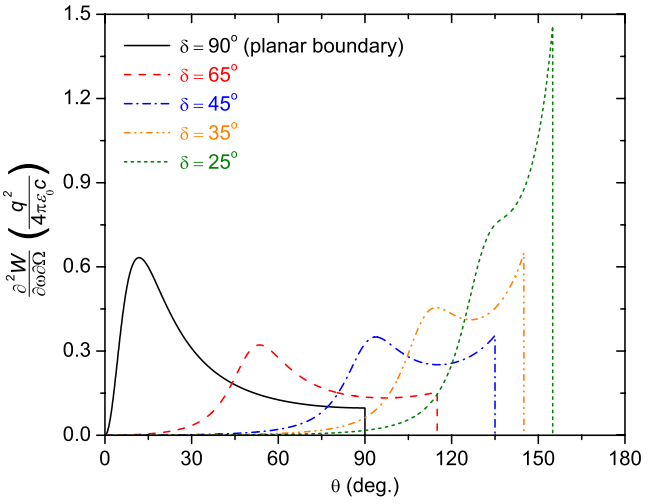

FIG. 3. (Color online) Angular spectral brightness profile for several cone opening angles generated by a point charge moving with $\gamma=5$. The vertical lines represent the cutoff of the fields at the cone boundary $\theta=\pi-\delta$. The series of Eq. (23) has been truncated after 30 terms in the numerical evaluation.

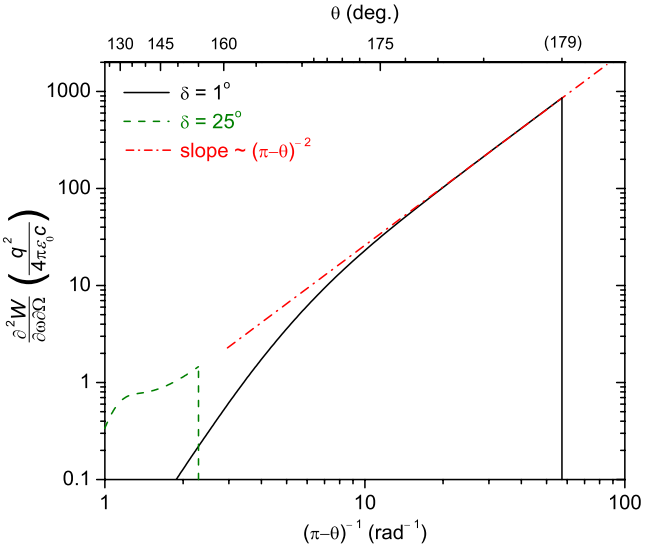

FIG. 4. (Color online) Angular spectral brightness profile near the cone boundary for a narrow-angle cone ($\delta=1°$). As a reference, the spectral brightness for a 25° cone has been plotted in both Fig. 3 and this figure. See also the comments below Fig. 3.

First, however, the numerical evaluation of Eqs. (23) and (24) for the spectral brightness and intensity will be presented in Sec. IV.

IV. NUMERICAL RESULTS

In Fig. 3 the spectral brightness [Eq. (23)] has been plotted for several values of the cone opening angle. For the charge velocity a relativistic factor of $\gamma\equiv(1-\beta^2)^{-1/2}=5$ has been taken. The series has been truncated after 30 terms in each case. The same truncation has been used in the remaining figures of this paper.

Apparent from Fig. 3 is that (i) the brightness profile contains a "specular" peak near $\theta=\pi-2\delta$, which moves toward the cone boundary as the opening angle decreases; (ii) as the opening angle decreases, the brightness profile develops a "surface" peak at the cone boundary; and (iii) this surface peak rapidly grows with decreasing opening angle and dominates the specular peak when $\delta<25°$.

The first radiation peak mentioned above is called specular since it is analogous to the specular reflection that would be observed at $\theta=\pi-2\delta$ if free electromagnetic radiation would be axially incident on the cone instead of a point charge. In the present case, however, the incident Coulomb field propagates in the negative z direction with a speed less than that of light. Therefore a Fourier decomposition of the field differs somewhat from a superposition of free e.m. waves with the wave number $k=\omega/c$ causing the deviation of the specular peak from the angle $\pi-2\delta$. Indeed, the specular peak tends to this angle when high values of γ are chosen.

The development of the surface peak with decreasing opening angle clearly shows the result of Sec. III C that the spectral brightness becomes peaked near the cone boundary in the narrow-angle cone limit. To study the surface peak in this limit, the spectral brightness has been plotted on a doubly logarithmic scale in Fig. 4 for a half opening angle of $\delta=1°$. Note from the scales that the peak height has increased very rapidly as compared to the $\delta=25°$ case. Also, the peak is very narrow with a full width at half maximum (FWHM) of about 0.5°. The peak shows the asymptotic narrow-angle cone behavior given by Eq. (34), which is indicated in Fig. 4 by the red line (dash-dot). The estimate [Eq. (31)] for the left bound of the regime that is dominated by the surface peak gives $\theta_c=154°$ for $\delta=1°$. Indeed, around this value of θ the surface peak shown in Fig. 4 rapidly grows larger than unity and starts to dominate the brightness profile. The $\propto(\pi-\theta)^{-2}$ behavior sets in at somewhat larger angles since Eq. (31) is a lower estimate.

As has been discussed in Sec. II, to estimate the amplitude of SPPs the transition radiation field will excite, the quantity of interest is the magnetic field at the cone boundary. Thus, in the light of terahertz SPP generation by transition radiation, another very important advantage of the cone geometry is evident: the excited SPPs can be increased by orders of magnitude by tapering the tip into a very narrow cone. This is illustrated once more in Fig. 5, in which the spectral brightness evaluated at the cone boundary has been plotted as a function of half opening angle. The spectral brightness increases by 4 orders of magnitude over the range $\delta=90°\rightarrow\delta=1°$, corresponding to an increase of 2 orders of magnitude in the magnetic field and SPP amplitude.

Of interest as well is the spectral intensity [Eq. (24)]. This quantity has been plotted in Fig. 6 as a function of half opening angle. The intensity increases only by a factor of 4 over the range $\delta=90°\rightarrow\delta=1°$, in contrast to the rapid growth of the brightness near the cone boundary. Thus, the primary effect of a small opening angle is not so much that more radiation energy is generated but rather that the radiation strongly concentrates into a narrow solid angle grazing the cone boundary.

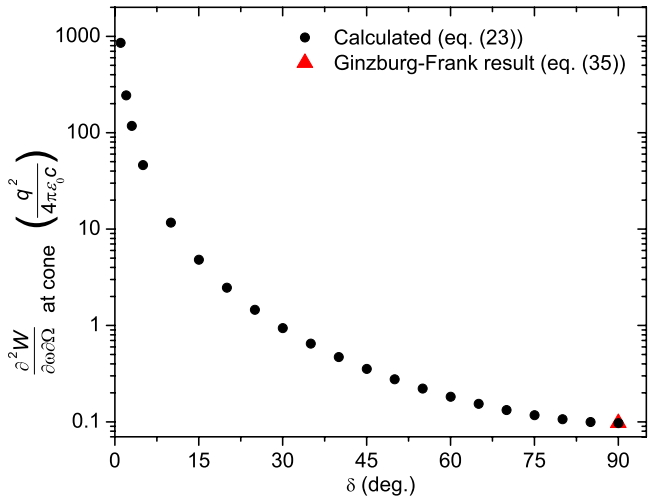

FIG. 5. (Color online) Spectral brightness at the cone boundary as a function of half cone opening angle generated by a point charge moving with $\gamma=5$. The Ginzburg-Frank result Eq. (35) for a planar boundary has been plotted as well.

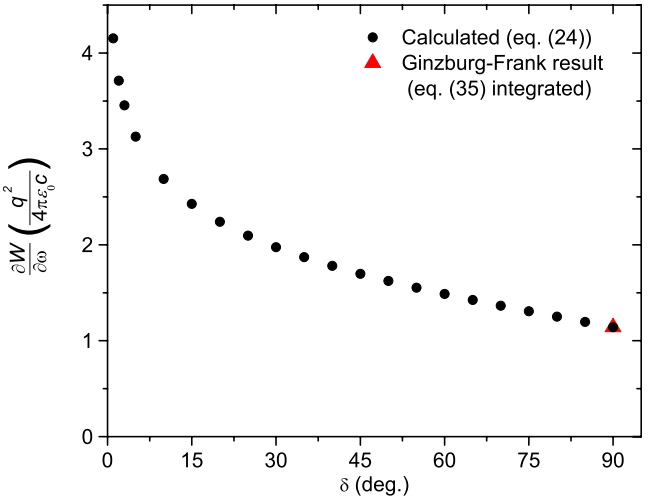

FIG. 6. (Color online) Spectral intensity as a function of half cone opening angle generated by a point charge moving with $\gamma=5$. The Ginzburg-Frank result for a planar boundary given by Eq. (35) integrated over the angular coordinates has been plotted as well.

V. VALIDATION

In order to validate the results obtained in the previous sections, we compare result (23) for the spectral brightness with results obtained by alternative methods in both the limit of a large cone opening angle (planar boundary or $\delta=90°$) and the limit of a narrow cone opening angle (semi-infinite line or $\delta\to 0$).

A. Planar boundary limit

The transition radiation field generated by a point charge that is normally incident on a planar boundary between different media was calculated in closed exact form by Ginzburg and Frank.[33] In the special case that one of the media is a perfect conductor and the other is a vacuum, their result for the spectral brightness reduces to

$$\frac{\partial^2 W}{\partial\omega\,\partial\Omega}=\frac{q^2}{4\pi\epsilon_0 c}\left(\frac{\beta\sin\theta}{\pi(1-\beta^2\cos^2\theta)}\right)^2. \tag{35}$$

A plot of this expression as a function of θ proves identical to the black solid graph in Fig. 3 for the planar boundary. Accordingly, the Ginzburg-Frank results that are shown as well in Figs. 5 and 6 are equal to the corresponding values calculated with our theory. Thus, result (23) for the spectral brightness is in exact agreement with the closed-form result (35) of Ginzburg and Frank.

B. Semi-infinite line limit

One approximate method to obtain the scattered electromagnetic field, which results if some known field is incident on a conducting object, is the physical theory of diffraction (PTD) method. The method is commonly used in antenna theory.[56] The primary approximation in the method is to suppose that the surface current density **K** on the conductor surface satisfies the boundary condition,

$$\mu_0\boldsymbol{K}=2\boldsymbol{n}\times\boldsymbol{B}_{\rm in}\ \text{ rather than }\ \mu_0\boldsymbol{K}=\boldsymbol{n}\times\boldsymbol{B}_{\rm tot}, \tag{36}$$

where $\boldsymbol{B}_{\rm in}$ is the (unperturbed) incident magnetic field and $\boldsymbol{B}_{\rm tot}$ is the total (incident plus scattered) magnetic field. Thus, the magnetic-field contribution at the surface induced by the surface current is assumed to be equal to the incident field. From the resulting approximate surface current distribution, the scattered electromagnetic fields may be calculated by evaluation of the standard electromagnetic vector potential.

The PTD method has been subjected to some criticisms.[56] The most important objection in the case of a cone as a scatterer is that the curvature of the surface is infinite at the tip, which in general makes Eq. (36) a poor approximation. However, the method has been successfully applied to accurately calculate the radar cross section of a narrow-angle semi-infinite cone.[53,57,58] Moreover, rigorous expansions of the surface current density exist, which are in good agreement with the PTD approximation near the cone tip.[59] Therefore, we proceed by applying the PTD method to the transition radiation problem and the results will show to be in perfect agreement with the results obtained in Sec. III C.

In the present case, the incident field $\boldsymbol{B}_{\rm in}$ is that generated by the moving point charge extended into the region $z<0$. The current distribution $\boldsymbol{J}$ of this charge is given by Eq. (16). Now, the current $\boldsymbol{J}$ generates $\boldsymbol{B}_{\rm in}$, and this field in turn generates the current $\boldsymbol{K}$ according to Eq. (36). Because of the symmetry that both currents $\boldsymbol{J}$ and $\boldsymbol{K}$ are confined to the z axis, it follows from Eq. (36) that simply

$$\boldsymbol{K}=2\boldsymbol{J},\quad z<0, \tag{37}$$

which is the current of a uniformly moving point charge $2q$. Now, the *total* electric far field is the radiation field produced by $\boldsymbol{K}$ at $z<0$ and $\boldsymbol{J}$ at $z>0$ *combined*. From this combination we may remove a common charge q moving along the complete z-axis, since the latter will not radiate at all. Thus, the effective radiation source reduces to a point charge q moving along the negative z axis and surrounded by free space. This

confirms the first contribution predicted at the end of Sec. III C.

To obtain the fields in some more detail, we consider the current distribution $I(z)$ of the effective source, which is

$$I(z) = -(2\pi)^{-1/2} q e^{-i\frac{k}{\beta}z}, \quad z < 0. \tag{38}$$

Note that $I(z)$ has the units of a Fourier transformed current. One may proceed by calculation of the vector potential generated by this current distribution, which involves transformation to the k domain and contour integration techniques.[60] However, the electromagnetic fields can be obtained directly in a more elegant way, by recognizing Eq. (38) as the current distribution of a linear traveling wave antenna of the slow type[61] with one of the end points placed at infinity. Traveling wave antennas carry a linearly phased current, as given by the factor $e^{-i\frac{k}{\beta}z}$, while "slow" refers to the fact that the propagation velocity βc is less than that of light in vacuum. Recently, a similar antenna model has been successfully used to describe the radiation from a metal tip coupled to terahertz pulses generated with a photoconductive switch.[62] An important property of traveling wave antennas is that they generate two distinct electromagnetic field contributions, namely, (i) they carry a radially evanescent electromagnetic field along their length, that is, a surface wave; (ii) they radiate from their end points only.

Regarding the current [Eq. (38)] as a limiting case of a slow wave antenna, the first of these contributions carries energy into an infinitesimally small solid angle around $\theta = \pi$. This contributes an additional peak to the spectral brightness profile at $\theta = \pi$ that is infinitesimally thin and infinitely high. This confirms the second property predicted at the end of Sec. III C.

Summarizing, by qualitative arguments the Green's-function method of Sec. III agrees with the PTD method and antenna theory used above. As an additional and a more quantitative check, we now calculate the spectral brightness using the antenna model.

Figure 7 shows a linear slow wave antenna with a current distribution $I(z) = I_0 e^{-i\frac{k}{\beta}z}$ and with the end points at $z = \pm L/2$, radiating in the direction θ. The electric radiation field in the far zone is given by[61]

$$\boldsymbol{E}_T = -I_0 \frac{\mu_0 c}{4\pi} \frac{e^{ikr}}{r} \frac{\beta \sin\theta}{1+\beta\cos\theta} \cdot \left(e^{ik\frac{L}{2}(\cos\theta+\beta^{-1})} - e^{-ik\frac{L}{2}(\cos\theta+\beta^{-1})}\right). \tag{39}$$

Now, the traveling wave $e^{-i\frac{k}{\beta}z}$ along the antenna gives a harmonic excitation of the end point in $z = \pm L/2$ with a phase of $e^{\mp i\frac{kL}{2\beta}}$ with respect to the origin so that it will radiate spherical waves with this phase. The waves from both end points subsequently add in the far field with an additional phase $e^{\mp i\frac{kL}{2}\cos\theta}$ due to the path difference induced by the orientation of the antenna with respect to the direction of propagation. The different phase factors in the two field contributions are indicated in Fig. 7. Observe in Eq. (39) that the phase factors in the second line correspond exactly to those just described so that the first line may be interpreted as the

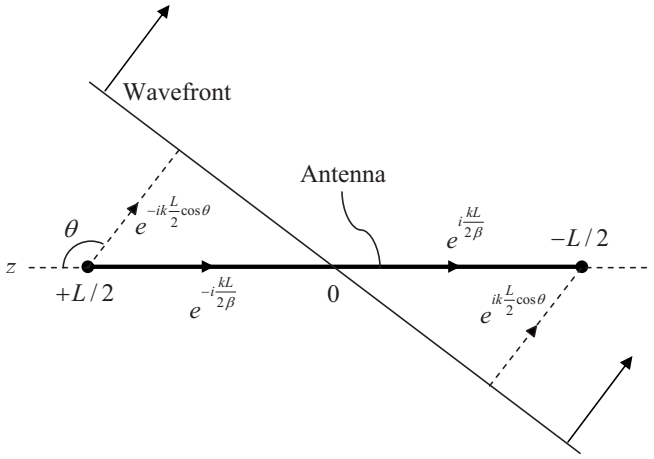

FIG. 7. Linear slow wave antenna with the end points at $z = \pm L/2$ radiating in the direction θ. Both end points radiate spherical waves, which acquire mutual phase differences at the shown wave front due to different optical path lengths. The direction of wave propagation along the different paths has been indicated by arrowheads together with the associated phase factor introduced in field expression (39).

radiation generated by a single end point. This is also noted in Ref. 60 for the case of a strip carrying a traveling wave. From the symmetry of the problem and the fact that the first line of Eq. (39) changes sign under the substitution $(\beta, \theta) \rightarrow (-\beta, \pi - \theta)$, the end points have equal radiation patterns but with opposite sign, hence the minus sign in the second line.

Returning to the semi-infinite antenna represented by current (38), only the radiation from the end point at $z = 0$ contributes to the far field at observation angles $\theta \neq \pi$ since the other end point is placed at an infinite distance. From Eq. (39) with $I_0 \equiv -(2\pi)^{-1/2} q$, the electric field in the far zone is

$$\boldsymbol{E}_T = \frac{\mu_0 q c}{2(2\pi)^{\frac{3}{2}}} \frac{e^{ikr}}{r} \frac{\beta \sin\theta}{1+\beta\cos\theta}. \tag{40}$$

Applying Eqs. (20)–(22) to this field yields the spectral brightness,

$$\frac{\partial^2 W}{\partial\omega\,\partial\Omega} = \frac{q^2}{4\pi\epsilon_0 c}\left(\frac{\beta\sin\theta}{2\pi(1+\beta\cos\theta)}\right)^2. \tag{41}$$

Now, Eq. (39) gives the free-space radiation field and does not include the surface wave traveling along the antenna. Therefore, in order to make a proper comparison of Eq. (41) with the result Eq. (23) obtained by the Green's-function method, we have to consider the latter in the limit $\delta \rightarrow 0$ and take the free-space radiation part only. In terms of the regular regime $0 < \theta < \theta_c$ and the regime $\theta_c < \theta < \pi$ where the brightness is peaked considered in Sec. III C, this is equivalent to letting θ_c approach π as $\delta \rightarrow 0$ and remove the resulting radiation peak along the z axis. This is easily effected by enforcing $\sigma_0 \equiv 0$ in Eq. (28), that is, by using in expansion (23) integer degree Legendre functions. The resulting adapted series has been plotted in Fig. 8. Indeed, the

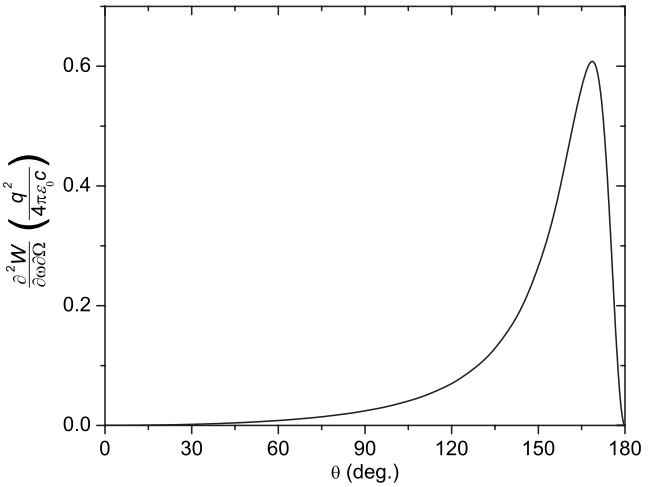

FIG. 8. Angular spectral brightness profile in the limit that $\delta \to 0$. The limit has been taken by choosing the integers for the set of eigenvalues $\{\sigma\}$ in the series of Eq. (23). A point charge moving with $\gamma=5$ has been assumed and the series has been truncated after 30 terms in the numerical evaluation.

remaining spectral brightness thus obtained is exactly the same as that given by Eq. (41).

In summary, the Green's-function result for the spectral brightness is in exact agreement with both the Ginzburg-Frank result for the planar boundary limit and the PTD method for the narrow-angle cone limit. Therefore we are confident that the results obtained for the intermediate opening angles are reliable.

VI. EXTENSION TO ELECTRON BUNCHES

In Sec. I of this paper we proposed to excite very strong SPPs using bunched electrons rather than a single point charge. To study the effect of such an extended source charge, we now replace the point charge in Fig. 2 by a general charge distribution that moves as a whole toward the cone tip without deforming, that is, by an electron bunch. Since different parts of the bunch will generate transition radiation at different times, the extent of the bunch in both the longitudinal and transverse directions will determine the magnitude of the radiation field by coherence effects. Below, the effects of the longitudinal and transverse extent of the bunch will be calculated separately. In the next section, the results will be combined to estimate the radiation field and SPP intensities generated by an electron bunch that can be readily obtained with present technology.

A. Bunches of finite length

The point charge of Fig. 2 passes the cone boundary at the origin at time $t=0$. If instead a point charge is considered that passes the origin at some other time $t_1 \neq 0$, Eqs. (16) and (18) for the current distribution and electric field, respectively, are multiplied by a phase factor $e^{i\frac{k}{\beta}z_1}$, where $z_1 = \beta c t_1$ is the position of the charge on the z axis at $t=0$. Therefore, composing at $t=0$ a line charge distribution $\lambda(z)$ on the z axis from individual point charges and adding their electric fields yields

$$\boldsymbol{E}_T = \frac{1}{q}\left(\int_{-\infty}^{\infty} \lambda(z_1) e^{i\frac{k}{\beta}z_1} dz_1\right)\boldsymbol{E}_{T0} \equiv F_L \boldsymbol{E}_{T0}. \tag{42}$$

Here, $\boldsymbol{E}_T$ is the electric transition radiation field generated by the line distribution, q is the total charge of the distribution, and $\boldsymbol{E}_{T0}$ is the field that would be produced by a point charge of magnitude q. The quantity F_L appears frequently in radiation problems and is called the (longitudinal) form factor.[63] From Eqs. (20)–(22), the spectral brightness produced by the charge distribution is

$$\frac{\partial^2 W}{\partial \omega\, \partial \Omega} = |F_L|^2 \frac{\partial^2 W_0}{\partial \omega\, \partial \Omega}, \tag{43}$$

where $\partial^2 W_0 / \partial\omega \partial\Omega$ is the spectral brightness produced by a point charge of magnitude q. Evidently, the form factor decreases rapidly as $|kz_1/\beta|$ grows larger than unity in the integral of Eq. (42), corresponding to incoherent contributions to the radiation field from the different parts of the charge distribution. If, on the other hand, the distribution is not much longer than a single wavelength of interest, the radiation contributions add coherently, leading to very strong electric fields.

B. Bunches of finite transverse extent

To study the effect of the transverse extent of the charge distribution impinging on the cone tip, we consider an infinitesimally thin and homogeneously filled disk of charge with radius a and total charge q with its center at the z axis. The Fourier transformed current density of this disk is

$$\boldsymbol{J}(\omega) = \frac{-q}{\sqrt{2\pi}} \frac{1}{\pi a^2} e^{-i\frac{k}{\beta}z} \Theta(a-\rho)\boldsymbol{e}_z, \tag{44}$$

where Θ denotes the Heaviside step function. Substitution of this expression and the dyadic Green's function (17) in Eq. (13) yields an expression for the transverse electric field generated by the charged disk. Similar to the electric field generated by a point charge considered in Appendix D, in the far zone $kr \to \infty$ this expression reduces to

$$\boldsymbol{E}_T(\boldsymbol{r}) \approx \frac{\mu_0 \omega q}{\sqrt{2\pi}} \frac{e^{ikr}}{kr} \sum_{\sigma} \frac{\alpha_\sigma^2 e^{-i\sigma\frac{\pi}{2}}}{\sigma(\sigma+1)} Q_\sigma(\beta, ka) P_\sigma^1(\cos\,\theta)\boldsymbol{e}_\theta, \tag{45}$$

where now

$$Q_\sigma(\beta, ka) \equiv \frac{k}{\pi a^2} \int\int\int_{V_0} e^{-i\frac{k}{\beta}z_0} \boldsymbol{e}_z \cdot \boldsymbol{N}_\sigma^{(1)}(\boldsymbol{r}_0) dV_0. \tag{46}$$

Because of the step function in Eq. (44), the integration volume V_0 in Q_σ is confined to a semi-infinite cylinder with a conical cut out, as is shown in Fig. 9. In Appendix E, the quantity Q_σ is analyzed further. It is shown that Eq. (46) can be reduced to a one-dimensional integral using the properties of the functions $\boldsymbol{N}_\sigma$. The expression thus obtained is checked by taking the limit $ka \to 0$, which yields the correct equiva-

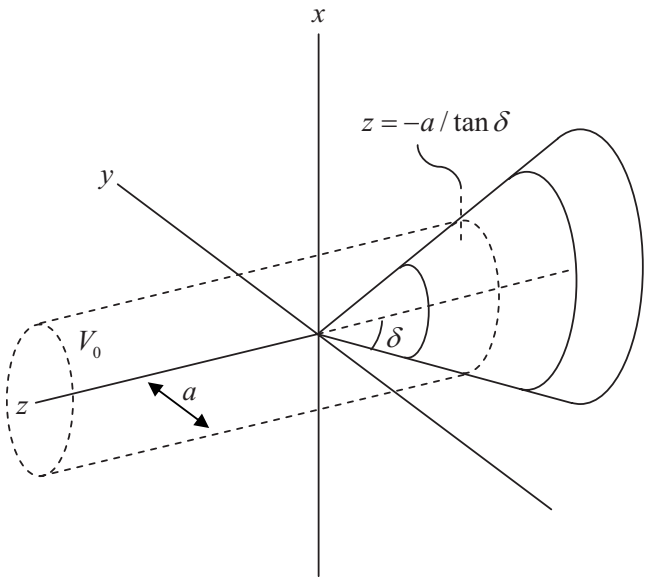

FIG. 9. Integration volume V_0 to be used in Eq. (46).

lent expression for a point charge. Finally, the remaining integration path is deformed in the complex s plane in order to substitute exponential behavior for oscillatory behavior of the integrand along the path, which enables efficient numerical evaluation of Eq. (46). For any choice of the cone opening angle and the dimensionless disk size ka, Eq. (45) now permits numerical evaluation of the electric far field. As usual, Eqs. (20)–(22) translate the electric field to the spectral brightness. As an example, Fig. 10 shows the spectral brightness profile thus obtained for a $\delta=45°$ cone and several values of ka. As the disk grows larger than about $a=k^{-1}=\lambda/(2\pi)$, radiation from different parts of the disk start to become incoherent, decreasing the spectral brightness magnitude. The surface peak decreases more rapidly with ka than the specular peak, which can be observed for other opening angles as well.

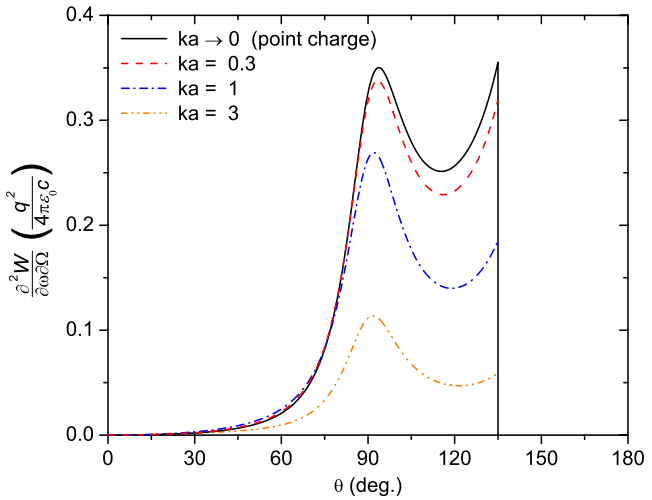

FIG. 10. (Color online) Angular spectral brightness profile for a $\delta=45°$ cone and several disk sizes ka. The same conditions as in Fig. 3 have been used. The black solid curve ($ka\to 0$) has been obtained using the point charge result Eq. (23).

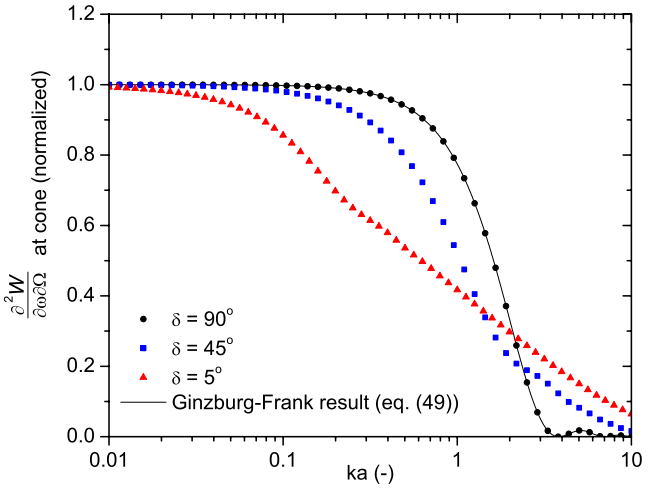

FIG. 11. (Color online) Spectral brightness at the cone boundary as a function of dimensionless disk size ka. For the velocity of the disk a relativistic factor of $\gamma=5$ has been assumed. The curves have been normalized to their corresponding point charge result shown in Fig. 5. The Ginzburg-Frank result for a planar boundary adjusted by the disk form factor [Eq. (49)] has been plotted as well (solid line).

To study the effect of the disk size on the spectral brightness in more detail, the spectral brightness at the cone boundary and the spectral intensity have been plotted as a function of ka in Figs. 11 and 12, respectively, for several values of the opening angle. In the case of a planar boundary, extending a point charge to a disk has little effect on the considered quantity in both figures until the disk radius grows larger than about $ka=1$, after which the curves quickly decrease. One effect of choosing a smaller opening angle is that the coherence starts to break down at smaller disk radii, which is a disadvantage of the use of small opening angle cones. However, this effect is more than compensated by the

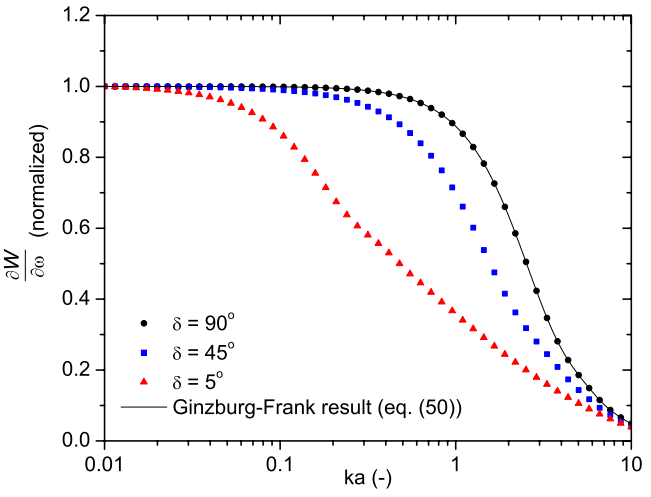

FIG. 12. (Color online) Spectral intensity as a function of dimensionless disk size ka. For the velocity of the disk a relativistic factor of $\gamma=5$ has been assumed. The curves have been normalized to their corresponding point charge result shown in Fig. 6. The Ginzburg-Frank result for a planar boundary adjusted by the disk form factor [Eq. (50)] has been plotted as well (solid line).

greatly increased spectral brightness shown in Fig. 5. Moreover, for $ka > \sim 1$, small opening angle cones yield more coherent radiation compared to a planar boundary. This can be a significant advantage when it is technologically difficult to reduce the transverse bunch size.

As before, the results for the planar boundary $\delta=90°$ can be checked with the Ginzburg-Frank result Eq. (35). Analogous to the effect of a longitudinal extent of the charge distribution shown by Eq. (43), in the case of the disk the spectral brightness should by multiplied by a transverse form factor $|F_T|^2$ with[63]

$$F_T = \frac{1}{q}\int_0^{2\pi}\int_0^{\infty} \sigma(\rho,\phi) e^{ik_r \rho \cos\phi} \rho d\rho d\phi, \tag{47}$$

where $\sigma(\rho,\phi)$ is the surface charge distribution of the disk and $k_r = k \sin\theta$ is the radial component of the wave vector of the radiation under consideration. For the disk considered here, Eq. (47) yields

$$F_T = \frac{2J_1(ka \sin\theta)}{ka \sin\theta}, \tag{48}$$

where J is the cylindrical Bessel function. Thus, Ginzburg-Frank theory predicts a spectral brightness at the cone boundary $\theta=\pi/2$ proportional to

$$\frac{\partial^2 W}{\partial\omega\,\partial\Omega} \propto \left(\frac{J_1(ka)}{ka}\right)^2, \tag{49}$$

while the spectral intensity is proportional to

$$\frac{\partial W}{\partial\omega} \propto \int_0^{\pi/2} \left(\frac{J_1(ka \sin\theta)}{ka(1-\beta^2\cos^2\theta)}\right)^2 \sin\theta d\theta. \tag{50}$$

In Figs. 11 and 12 these results have been plotted as well and they are in excellent agreement with the numerical results.

C. Three-dimensional bunches

Combining the above results for the longitudinal and transverse extent of the source charge distribution to obtain the transition radiation from three-dimensional electron bunches is straightforward. Consider a bunch with a cylindrically symmetric charge-density distribution $\tau(\rho,z)$ at time $t=0$. Of course, the bunch may be thought of as composed of transverse slices of infinitesimal thickness dz and charge equal to,

$$dq(z) = dz \cdot 2\pi \int_0^{\infty} \tau(\rho,z)\rho d\rho \equiv \lambda_{\text{eff}}(z) dz, \tag{51}$$

and for each one of them the electric far field can be calculated by the method of Sec. VI B. Note that any charge distribution of the slice other than homogeneous will introduce additional factors in the integrand of Eq. (46), requiring additional numerical effort. The resulting field of the slice will always be less than that of a point charge of equal magnitude dq due to the extent of the charge within the slice. To obtain the electric field produced by the complete bunch, the fields of the individual slices must be added. While doing so, the phase differences due to the longitudinal positions of the individual slices within the bunch have to be accounted for as was done in Eq. (42). Combining Eqs. (45) and (51) and including a longitudinal phase factor yields the electric far field of the bunch,

$$\boldsymbol{E}_T(\boldsymbol{r}) \approx \frac{\mu_0 \omega q}{\sqrt{2\pi}} \frac{e^{ikr}}{kr} \boldsymbol{e}_\theta \sum_\sigma \frac{\alpha_\sigma^2 e^{-i\sigma\frac{\pi}{2}}}{\sigma(\sigma+1)} P_\sigma^1(\cos\theta) \cdot \int_{-\infty}^{\infty} Q_\sigma(z_1) \times \frac{\lambda_{\text{eff}}(z_1)}{q} e^{i\frac{k}{\beta}z_1} dz_1. \tag{52}$$

Here, q is the charge of the whole bunch and $Q_\sigma(z_1)$ is an integral similar to Eq. (46) that accounts for the transverse extent of charge within the slice at $z=z_1$ in the bunch. In the case that each transverse cross section is a homogeneously charged hard-edged disk as in the previous section, $Q_\sigma(z_1) \equiv Q_\sigma[\beta, ka(z_1)]$ is given exactly by Eq. (46), where $a(z_1)$ is the radius of the slice at $z=z_1$. If in addition each slice is equal, the bunch has a somewhat artificial form of a hard-edged homogeneously charged cylinder with radius a and some length $2b$. In this case Q_σ becomes independent of z_1 so that Eq. (52) reduces to Eq. (45) multiplied by an effective longitudinal form factor $F_{L,\text{eff}}$. The latter is given by Eq. (42) with $\lambda = \lambda_{\text{eff}}$ and equals

$$F_{L,\text{eff}} = \sin c\left(\frac{kb}{\beta}\right). \tag{53}$$

VII. OBTAINABLE SPPs IN THE TIME DOMAIN

Let us now return to the experimental setup of Fig. 1 that we propose to generate SPPs on a wire. In Secs. III–VI we have modeled the metal tip of the wire by a semi-infinite perfectly conducting cone and showed how the radiation field generated by charge impinging on it can be calculated. Now, we will choose some realistic electron bunches and apply the theory to these bunches. In Sec. II we showed that the field strength at the cone boundary of a perfect metal thus obtained may be identified with the amplitude of the generated SPP propagating along the physical metal tip of Fig. 1, as long as conditions (5)–(7) hold.

As a realistic setup we choose a copper wire with radius $R=0.5$ mm tapered into a $\delta=5°$ tip, which is sharp enough to benefit from the strong increase in the field amplitude shown in Fig. 5 but which is still easy to manufacture. For terahertz frequencies, it is easily verified that conditions (5) and (6) hold at the position where the conical tip smoothly evolves into the cylindrical wire [i.e., at $r=R/\sin\delta$ or $|z| = R/\tan\delta$ in Eqs. (5) and (6)]. Analysis of the longitudinal wave vector $k_z(a)$ as a function of local radius $a=|z|\tan\delta$ shows that also condition (7) holds at this position.[3] So if in the setup of Fig. 1 the tip smoothly evolves into the wire, we can estimate the field strength of the generated SPPs propagating along the wire by evaluating our theory at radial position $r=R/\sin\delta$.

For the bunch form we choose homogeneously charged hard-edged ellipsoids. Theoretically, such "waterbag" bunches are the ideal particle distributions for controlled

high-brightness charged particle acceleration. Because of their linear internal fields, they do not suffer from brightness degradation caused by space-charge forces.[64,65] A practical recipe has been developed, which results in almost ideal ellipsoidal bunches[45–48] using a table-top setup. The bunches are characterized by their charge q, their transverse half axis a, and their longitudinal half axis $b=\beta cT/2$. We consider three bunches: (1) a "conventional" bunch with $q=100$ pC, $T=500$ fs, and $a=200$ μm that we can presently make in the laboratory; (2) a "short" bunch with $q=100$ pC, $T=100$ fs, and $a=140$ μm. Detailed numerical simulations have shown that such a bunch may readily be obtained by longitudinal compression of bunch 1 using a two-cell booster compressor;[47] and (3) a "short and slim" bunch with $q=100$ pC, $T=100$ fs, and $a=50$ μm that is obtained by additional compression of bunch 2 in the transverse direction, which may be achieved in the near future.

For the three bunches above, we have calculated the electric field as a function of frequency generated at the cone boundary a distance $r=R/\sin\delta$ from the cone tip. For this purpose the bunches were approximated by 100 cylindrical slices so that the integrals in Eq. (52) were approximated by summations over the slices. To validate the numerical results, we compared the calculated spectra $E_{T\theta}(\omega)$ with those generated by cylindrical bunches with the same parameters q, a, and b. The latter electric fields are given by the product of Eqs. (45) and (53). These fields may be seen as "worst case" approximations for those generated by the ellipsoidal bunches since the average distance between the charges within a cylindrical bunch is larger than that within the corresponding ellipsoidal bunch, leading to less coherent radiation. The calculated squared field amplitudes are shown in Fig. 13. The spectra have been normalized to the field E_0 generated at the same position $r=R/\sin\delta$ by a point charge of equal magnitude $q=100$ pC given by

$$E_0^2 \equiv \frac{\sin^2\delta}{2\epsilon_0 cR^2}\left.\frac{\partial^2 W}{\partial\omega\,\partial\Omega}\right|_{\theta=\pi-\delta}, \tag{54}$$

with $\partial^2 W/\partial\omega\partial\Omega$ given by Eq. (23). As expected, the field generated by an ellipsoidal bunch is greater than that of the corresponding cylindrical bunch for all frequencies. This difference is only slight, however, which means that the maximum transverse and longitudinal cross sections of the bunch are decisive for the coherence. The spectra are coherent up to the terahertz regime, which reflects the fact that the bunch dimensions have been brought down to the order of the 1 THz wavelength $2\pi k^{-1}\approx 300$ μm$\approx c\times 1$ ps by current technology.

In order to find the pulse form of the SPPs that will be measured in practice in the setup of Fig. 1, the inverse Fourier transforms of the electric fields of Fig. 13 have to be calculated. A rigorous treatment of this is beyond the scope of this paper. However, the field spectra raise the question whether the time-domain pulse is governed by the terahertz regime, that is, whether the spectra do indeed represent subpicosecond SPPs. In order to verify this, we approximate the inverse Fourier transform of the field spectra of Fig. 13. For this purpose the spectra are approximated by straight line segments, as is indicated in the inset of the figure. In Appendix F the inverse Fourier transform of these approximate spectra is calculated. This yields an estimate of the peak electric field $E(t)_{\max}$ of the SPP pulse at the wire surface and the pulse duration τ, which is defined as

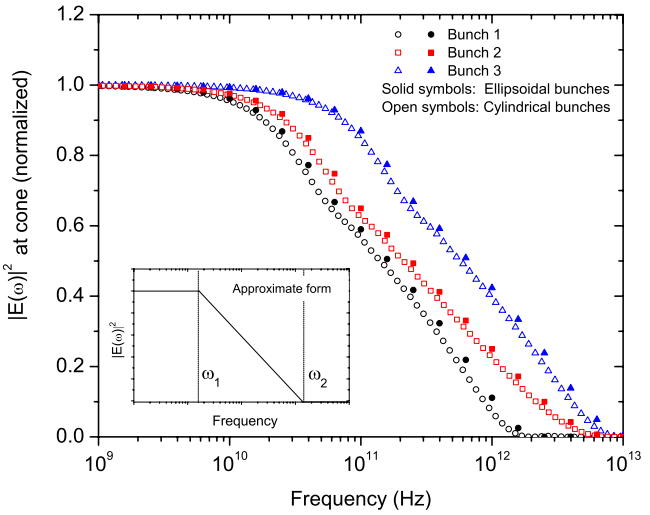

FIG. 13. (Color online) Squared electric-field amplitude at the cone boundary generated by the three bunches considered in Sec. VII (solid symbols) and that of corresponding cylindrical bunches with the same charge and dimensions (open symbols). A relativistic factor of $\gamma=5$ and a cone opening angle of $\delta=5°$ have been assumed. The curves have been normalized to the field amplitude generated by a point charge of equal magnitude as the bunches. The inset shows the approximate form of the curves used in Sec. VII to make time-domain estimations.

$$\tau \equiv \frac{1}{E(t)_{\max}}\int_{-\infty}^{\infty} E(t)dt. \tag{55}$$

Table I shows the estimated peak electric field and duration of the SPP pulse as defined above generated by the three considered bunches. As can be seen, the SPP pulse is governed by the high-frequency part of the field spectra since $\tau<1$ ps. From the table, the potential of the method we propose to generate terahertz SPPs is clear. First, by using currently available electron bunches, it is possible to excite subpicosecond pulses, that is, SPPs with terahertz bandwidth can be generated on a wire. Second, these SPPs carry peak electric fields in the order of MV/cm. Such fields are several orders of magnitude higher than any SPP field that can cur-

TABLE I. Time-domain estimates of the peak SPP electric field $E(t)_{\max}$ [Eq. (F4)] and pulse duration τ [Eq. (F5)] using the parameters ω_1 and ω_2 in the field model [Eq. (F1)].

Bunch	ω_1 (THz)	ω_2 (THz)	$E(t)_{\max}$ (MV/cm)	τ (ps)
1	$1.1\cdot10^{-2}$	2.0	0.35	0.64
2	$1.3\cdot10^{-2}$	5.0	0.82	0.27
3	$4.7\cdot10^{-2}$	8.2	1.4	0.16

rently be obtained by coupling free-space terahertz radiation onto a wire.

VIII. CONCLUSION

In conclusion, we propose a method to excite terahertz SPPs on a wire by launching electron bunches onto a conically tapered end of the wire. We have calculated analytically the radiation field generated by these bunches assuming a perfectly conducting semi-infinite cone. We have linked the results to the electric-field strength and duration of the SPPs that are excited and propagate along the wire in a realistic setup. We have shown that, using currently available electron bunches, it is possible to generate subpicosecond SPP pulses with peak electric fields of the order of MV/cm on a 1-mm diameter wire.

Focusing of such MV/cm terahertz surface plasmon polaritons may yield electromagnetic terahertz fields that are both very strong and highly localized, enabling nonlinear terahertz experiments with subwavelength spatial resolution.

ACKNOWLEDGMENTS

We would like to thank A. G. Tijhuis and B. P. de Hon for their valuable suggestions.

APPENDIX A: APPROXIMATE SPP FIELD IN CONICAL GEOMETRY

Using the eikonal method to approximate the SPP electric field in a conical geometry,[9] it is recognized that a thin slice of the cone at $z=z_0<0$ resembles part of a cylinder with radius $a=|z_0|\tan\delta$ so that locally the SPP fields resemble the fields of a surface wave propagating along such a cylinder. Hence, the SPP electric field in the conical geometry is approximated by

$$\boldsymbol{E}_{\mathrm{SPP}}(\boldsymbol{r}) = \boldsymbol{E}_{\mathrm{cyl}}(\boldsymbol{r}) e^{i\psi(z)}, \tag{A1}$$

where $\psi(z)$ is a phase function to be determined and $\boldsymbol{E}_{\mathrm{cyl}}(\boldsymbol{r})$ is the field of a surface wave along a cylinder with radius a. The latter is given in cylindrical coordinates (ρ,ϕ,z) by[66]

$$\begin{pmatrix} E_{\mathrm{cyl},\rho} \\ E_{\mathrm{cyl},\phi} \\ E_{\mathrm{cyl},z} \end{pmatrix} = \begin{pmatrix} k_z I_1(\kappa\rho) \\ 0 \\ i\kappa I_0(\kappa\rho) \end{pmatrix} \frac{c}{\epsilon_r k} \frac{B_0(z_0)}{I_1[\kappa a(z_0)]}, \tag{A2}$$

in which I_m denotes the mth-order modified Bessel function of the first kind, ϵ_r is the relative permittivity of the cylinder material, $k=\omega/c$ is the vacuum wave number, and B_0 is an amplitude with units of magnetic field. Like a, the latter may depend on the choice of z_0 as is indicated in Eq. (A2). The parameters k_z and κ are the propagation constant in the z direction and the radial attenuation factor, respectively, and are related as

$$\sqrt{k_m^2 - k_z^2} = i\sqrt{|k_m^2 - k_z^2|} \equiv i\kappa, \tag{A3}$$

with $k_m=\sqrt{\epsilon_r}k$ as the wave number in the cylinder material. For each radius a, the constant k_z can be determined solving a transcendental dispersion relation[66] that depends on ω and ϵ_r. For metals, applying the Drude model for the permittivity,[50] one can calculate that

$$k_z \approx k \quad \text{and} \quad \kappa \approx \frac{1-i}{k\Delta} \tag{A4}$$

at terahertz frequencies. Substituting these approximations into Eq. (A2) gives

$$\boldsymbol{E}_{\mathrm{cyl}} \approx (1-i)\sqrt{\frac{\omega}{2\mu\sigma}} e^{(1-i)\frac{\rho-a(z_0)}{\Delta}} B_0(z_0)\boldsymbol{e}_z \tag{A5}$$

for $a(z_0)\gg\Delta$. In the cone geometry, the SPP field will decrease as r^{-1} as it diverges from the cone tip so that a form $B_0\propto(z_0)^{-1}$ may be assumed for the field amplitude. Using this form and Eq. (A4), substitution of Eqs. (A1) and (A5) in Eq. (3) and differentiation show that Eq. (4) is an approximate solution of Eq. (3) provided that Eqs. (5)–(7) hold.

APPENDIX B: DERIVATION OF EQ. (13)

Any vector field can be written as the sum of the gradient of some scalar field and the curl of some vector field,[49] which are called the longitudinal and transverse part of the vector field, respectively. Applying the Helmholtz operator (∇^2+k^2) on a vector field does not change its longitudinal or transverse property. Similarly, the dyadic Green's function in Eq. (11) may be split into longitudinal and transverse components $\mathfrak{G}_{\mathrm{long}}$ and $\mathfrak{G}_T$, such that

$$\nabla\times\mathfrak{G}_{\mathrm{long}} = \nabla_0\times\mathfrak{G}_{\mathrm{long}} = \mathfrak{O}, \tag{B1}$$

$$\nabla\cdot\mathfrak{G}_T = \nabla_0\cdot\mathfrak{G}_T = \boldsymbol{0}, \tag{B2}$$

with $\mathfrak{O}$ as the zero dyadic. It can be shown that application of the Helmholtz operator on these dyadics gives[51]

$$(\nabla^2+k^2)\mathfrak{G}_{\mathrm{long}} = \mathfrak{L}(\boldsymbol{r},\boldsymbol{r}_0),$$

$$(\nabla^2+k^2)\mathfrak{G}_T = \mathfrak{T}(\boldsymbol{r},\boldsymbol{r}_0), \tag{B3}$$

where the dyadics on the right-hand side have the properties,

$$\int \mathfrak{L}\cdot\boldsymbol{X}(\boldsymbol{r}_0)d^3\boldsymbol{r}_0 = \boldsymbol{X}_{\mathrm{long}}(\boldsymbol{r}),$$

$$\int \mathfrak{T}\cdot\boldsymbol{X}(\boldsymbol{r}_0)d^3\boldsymbol{r}_0 = \boldsymbol{X}_T(\boldsymbol{r}),$$

$$\mathfrak{L}+\mathfrak{T} = \mathfrak{I}\delta^3(\boldsymbol{r}-\boldsymbol{r}_0), \tag{B4}$$

for any vector field $\boldsymbol{X}$. Taking the inner product of Eq. (8) with $\mathfrak{G}_T$ and that of Eq. (B3) with $\boldsymbol{E}(\boldsymbol{r}_0)$, subtracting, and integrating over the exterior cone volume V_0 gives

$$\int\int\int_{V_0} [\boldsymbol{E}(\boldsymbol{r}_0)\cdot\nabla_0^2\mathfrak{G}_T - \mathfrak{G}_T\cdot\nabla_0^2\boldsymbol{E}(\boldsymbol{r}_0)]dV_0$$

$$= \boldsymbol{E}_T(\boldsymbol{r}) - \int\int\int_{V_0} \mathfrak{G}_T\cdot[\epsilon_0^{-1}\nabla_0\rho(\boldsymbol{r}_0) - i\omega\mu_0\boldsymbol{J}(\boldsymbol{r}_0)]dV_0, \tag{B5}$$

where Eq. (B4) has been used. The left-hand side can be

written as an integral over the cone surface A_0 with Green's second theorem,[51] giving

$$\int\int_{A_0} [(\boldsymbol{n}\times\boldsymbol{E}_0)\cdot(\nabla_0\times\mathfrak{G}_T)-(\boldsymbol{n}\times\mathfrak{G}_T)\cdot(\nabla_0\times\boldsymbol{E}_0) + (\boldsymbol{n}\cdot\boldsymbol{E}_0)(\nabla_0\cdot\mathfrak{G}_T)-(\boldsymbol{n}\cdot\mathfrak{G}_T)(\nabla_0\cdot\boldsymbol{E}_0)]dA_0,$$

in which $\boldsymbol{E}(\boldsymbol{r}_0)$ has been abbreviated as $\boldsymbol{E}_0$. Since boundary conditions (9) and (12) apply at the cone surface and $\mathfrak{G}_T$ satisfies Eq. (B2), the first three terms in this surface integral vanish. Furthermore, using that $\nabla\cdot\boldsymbol{E}=\epsilon_0^{-1}\rho$, Gauss's theorem yields

$$\int\int_{A_0}(\boldsymbol{n}\cdot\mathfrak{G}_T)(\nabla_0\cdot\boldsymbol{E}_0)dA_0=\epsilon_0^{-1}\int\int\int_{V_0}\mathfrak{G}_T\cdot\nabla_0\rho(\mathbf{r}_0)dV_0$$

so that the last term in the surface integral cancels identically the contribution of the charge density in Eq. (B5). Therefore, Eq. (B5) reduces to Eq. (13).

APPENDIX C: DYADIC GREEN'S FUNCTION FOR CONICAL GEOMETRY

The dyadic Green's function that satisfies

$$(\nabla^2+k^2)\mathfrak{G}=(\nabla_0^2+k^2)\mathfrak{G}=\mathfrak{I}\delta^3(\boldsymbol{r}-\boldsymbol{r}_0), \tag{C1}$$

subject to the boundary condition,

$$\mathfrak{G}\times\boldsymbol{e}_\theta=\mathfrak{O},\quad \theta=\pi-\delta, \tag{C2}$$

is[51,52]

$$\mathfrak{G}(\boldsymbol{r},\boldsymbol{r}_0)=-ik(\mathfrak{G}_L+\mathfrak{G}_M+\mathfrak{G}_N), \tag{C3}$$

with

$$\mathfrak{G}_L=\sum_\sigma\sum_{m=0}^{\infty}\alpha_{\sigma m}^2\begin{cases}\boldsymbol{L}_{\sigma m}^{(1)}(\boldsymbol{r})\boldsymbol{L}_{\sigma m}^{(3)}(\boldsymbol{r}_0)\\ \boldsymbol{L}_{\sigma m}^{(1)}(\boldsymbol{r}_0)\boldsymbol{L}_{\sigma m}^{(3)}(\boldsymbol{r})\end{cases}, \tag{C4}$$

$$\mathfrak{G}_M=\sum_\nu\sum_{m=0}^{\infty}\frac{\alpha'^2_{\nu m}}{\nu(\nu+1)}\begin{cases}\boldsymbol{M}_{\nu m}^{(1)}(\boldsymbol{r})\boldsymbol{M}_{\nu m}^{(3)}(\boldsymbol{r}_0)\\ \boldsymbol{M}_{\nu m}^{(1)}(\boldsymbol{r}_0)\boldsymbol{M}_{\nu m}^{(3)}(\boldsymbol{r})\end{cases}, \tag{C5}$$

$$\mathfrak{G}_N=\sum_\sigma\sum_{m=0}^{\infty}\frac{\alpha_{\sigma m}^2}{\sigma(\sigma+1)}\begin{cases}\boldsymbol{N}_{\sigma m}^{(1)}(\boldsymbol{r})\boldsymbol{N}_{\sigma m}^{(3)}(\boldsymbol{r}_0)\\ \boldsymbol{N}_{\sigma m}^{(1)}(\boldsymbol{r}_0)\boldsymbol{N}_{\sigma m}^{(3)}(\boldsymbol{r})\end{cases}, \tag{C6}$$

where the upper rows apply when $r<r_0$ and the lower rows apply when $r>r_0$. The scale factors α are given by[54]

$$\alpha_{\sigma m}^{-2}=\int_0^{2\pi}\int_0^{\pi-\delta}|P_\sigma^m(\cos\theta)|^2\sin\theta d\theta d\phi = \frac{2\pi\sin\delta}{2\sigma+1}\left(\frac{\partial P_\sigma^m(\cos\theta)}{\partial\sigma}\frac{\partial P_\sigma^m(\cos\theta)}{\partial\theta}\right)\Bigg|_{\theta=\pi-\delta}, \tag{C7}$$

$$\alpha'^{-2}_{\nu m}=\int_0^{2\pi}\int_0^{\pi-\delta}\left|\frac{d}{d\theta}P_\nu^m(\cos\theta)\right|^2\sin\theta d\theta d\phi, \tag{C8}$$

where P_σ^m denotes the associated Legendre function of the first kind, degree σ, and order m. The vector functions constituting the dyadic products in Eqs. (C4)–(C6) are given in spherical components (e_r,e_θ,e_ϕ) by

$$\boldsymbol{L}_{\sigma m}^{(p)}(\boldsymbol{r})=\begin{pmatrix}\frac{d}{dr}j_\sigma^{(p)}(kr)P_\sigma^m(\cos\theta)\\ \frac{j_\sigma^{(p)}(kr)}{r}\frac{d}{d\theta}P_\sigma^m(\cos\theta)\\ im\frac{j_\sigma^{(p)}(kr)}{r}\frac{P_\sigma^m(\cos\theta)}{\sin\theta}\end{pmatrix}e^{im\phi}, \tag{C9}$$

$$\boldsymbol{M}_{\nu m}^{(p)}(\boldsymbol{r})=\begin{pmatrix}0\\ im\frac{P_\nu^m(\cos\theta)}{\sin\theta}\\ -\frac{d}{d\theta}P_\nu^m(\cos\theta)\end{pmatrix}j_\nu^{(p)}(kr)e^{im\phi}, \tag{C10}$$

$$\boldsymbol{N}_{\sigma m}^{(p)}(\boldsymbol{r})=\begin{pmatrix}\sigma(\sigma+1)\frac{j_\sigma^{(p)}(kr)}{kr}P_\sigma^m(\cos\theta)\\ \frac{1}{kr}\frac{d}{dr}[rj_\sigma^{(p)}(kr)]\frac{d}{d\theta}P_\sigma^m(\cos\theta)\\ \frac{im}{kr}\frac{d}{dr}[rj_\sigma^{(p)}(kr)]\frac{P_\sigma^m(\cos\theta)}{\sin\theta}\end{pmatrix}e^{im\phi}, \tag{C11}$$

in which $j_\sigma^{(p)}$ is the spherical Bessel function of the pth kind and order σ. Because the functions are periodic in the azimuthal direction, $m=0,1,2,\ldots$. The sets of eigenvalues $\{\sigma\}$ and $\{\nu\}$ are such that the Green's function satisfies boundary condition (C2). Consequently, they are the solutions of

$$P_\sigma^m(-\cos\delta)=0, \tag{C12}$$

$$\frac{d}{d\theta}P_\nu^m(\cos\theta)\Big|_{\theta=\pi-\delta}=0. \tag{C13}$$

Miscellaneous properties of the vector functions are

$$\nabla\times\boldsymbol{L}_{\sigma m}^{(p)}=0, \tag{C14}$$

$$\nabla\cdot\boldsymbol{M}_{\nu m}^{(p)}=\nabla\cdot\boldsymbol{N}_{\sigma m}^{(p)}=0, \tag{C15}$$

$$k\boldsymbol{N}_{\sigma m}^{(p)}=\nabla\times\boldsymbol{M}_{\sigma m}^{(p)}. \tag{C16}$$

Due to properties (C14) and (C15), Green's function (C3) can easily be split into a longitudinal part $\mathfrak{G}_{\text{long}}$ and transverse part $\mathfrak{G}_T$ as

$$\mathfrak{G}_{\text{long}}=-ik\mathfrak{G}_L, \tag{C17}$$

$$\mathfrak{G}_T=-ik(\mathfrak{G}_M+\mathfrak{G}_N). \tag{C18}$$

Since the current densities considered in this paper are independent of ϕ, terms having $m\neq0$ in the expansion of $\mathfrak{G}_T$ integrate to zero in Eq. (13). Moreover, the dyadic $\mathfrak{G}_M$ makes no contribution to the integral since $\boldsymbol{M}_{\nu m}\cdot\boldsymbol{J}=0$ for $m=0$. Therefore, the relevant Green's function to be used in Eq. (13) is given by Eq. (17).

APPENDIX D: ELECTRIC FIELD IN THE FAR ZONE

Substitution of Eqs. (16) and (17) in Eq. (13) yields

$$\boldsymbol{E}_T = \frac{\mu_0 \omega k q}{\sqrt{2\pi}} \sum_\sigma \alpha_\sigma^2 \cdot \left[\left(\int_0^r \frac{j_\sigma(kz_0)}{kz_0} e^{-i\frac{k}{\beta}z_0} dz_0 \right) \boldsymbol{N}_\sigma^{(3)}(\boldsymbol{r}) + \left(\int_r^\infty \frac{h_\sigma^{(1)}(kz_0)}{kz_0} e^{-i\frac{k}{\beta}z_0} dz_0 \right) \boldsymbol{N}_\sigma^{(1)}(\boldsymbol{r}) \right], \quad \text{(D1)}$$

where the vector functions $\boldsymbol{N}_\sigma$ are given by Eq. (C11). In the far field $kr \to \infty$, the third line of Eq. (D1) vanishes. Furthermore, the asymptotic form of the vector functions is

$$\boldsymbol{N}_\sigma^{(3)} \approx P_\sigma^1(\cos\theta) e^{-i\sigma\frac{\pi}{2}} \frac{e^{ikr}}{kr} \boldsymbol{e}_\theta, \quad kr \gg 1, \quad \text{(D2)}$$

so that in the far zone the electric field reduces to Eq. (18), in which the integral,

$$I_\sigma(\beta) = \int_0^\infty \frac{j_\sigma(kz_0)}{z_0} e^{-i\frac{k}{\beta}z_0} dz_0, \quad \text{(D3)}$$

is tabulated[67] and given by Eq. (19).

APPENDIX E: ANALYSIS OF Q_σ IN EQ. (46)

Using property (C16) of the $\boldsymbol{N}$ functions and Stokes's theorem, integration in the plane $z=z_0$ yields

$$\int_0^{2\pi} \int_0^a \boldsymbol{e}_z \cdot \boldsymbol{N}_\sigma^{(1)}(\boldsymbol{r}_0) \rho_0 d\rho_0 d\phi_0 = \frac{2\pi a}{k} \boldsymbol{e}_\phi \cdot \boldsymbol{M}_\sigma^{(1)}(\boldsymbol{r}_1), \quad \text{(E1)}$$

where the functions $\boldsymbol{M}_\sigma$ are given by Eq. (C10) with $m=0$ and $\nu \equiv \sigma$, and $\boldsymbol{r}_1$ denotes the spherical coordinates,

$$(r_1, \theta_1, \phi_1) = \left(\sqrt{z_0^2 + a^2}, \arccos \frac{z_0}{\sqrt{z_0^2 + a^2}}, \phi_1 \right).$$

Making use of identity (E1) and expression (C10), Eq. (46) reduces to

$$Q_\sigma = \frac{2}{ka} \int_{-ka/\tan\delta}^\infty e^{-i\frac{s}{\beta}} P_\sigma^1\left(\frac{s}{R}\right) j_\sigma(R) ds + \frac{2\tan\delta}{(ka)^2} P_\sigma^1(-\cos\delta) \int_{-ka/\tan\delta}^0 s e^{-i\frac{s}{\beta}} j_\sigma\left(\frac{-s}{\cos\delta}\right) ds, \quad \text{(E2)}$$

$$R \equiv \sqrt{s^2 + (ka)^2}, \quad \text{(E3)}$$

in which the substitution $s=kz_0$ has been applied. Note that the first line of this expression represents integration over a full semi-infinite cylinder and the second line represents integration over the conical cut-out that is subtracted from the integration volume.

As a check on Eq. (E2), the limit $ka \to 0$ will now be taken to obtain the equivalent expression for a point charge. From the power series of the Bessel function,[68] the second line of Eq. (E2) is proportional to $(ka)^\sigma$ as $ka \to 0$ so that it vanishes in the limit. In the first line, we use the identity[67]

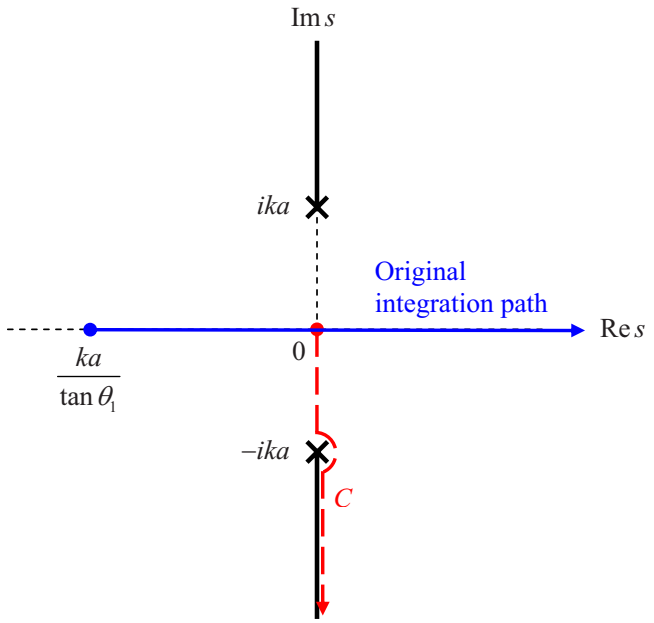

FIG. 14. (Color online) Original integration path in the first line of Eq. (E2) and contour C in Eq. (E5) in the complex s plane. The cuts and poles of $T_\sigma(s)$ are shown as well.

$$P_\nu^{\mu+2}(x) + 2(\mu+1)\frac{x}{\sqrt{1-x^2}} P_\nu^{\mu+1}(x) = (\nu-\mu)(\nu+\mu+1) P_\nu^\mu(x)$$

to rewrite

$$\frac{2}{ka} P_\sigma^1\left(\frac{s}{R}\right) = \frac{1}{s}\left[\sigma(\sigma+1) P_\sigma^0\left(\frac{s}{R}\right) - P_\sigma^2\left(\frac{s}{R}\right) \right].$$

Making use of this identity, taking the limit $ka \to 0$ of Eq. (E2) yields

$$\lim_{ka\to 0} Q_\sigma(\beta, ka) = \sigma(\sigma+1) I_\sigma(\beta), \quad \text{(E4)}$$

where $I_\sigma(\beta)$ is given by Eqs. (D3) and (19). With this, electric field (45) generated by the charged disk correctly reduces to field (18) generated by a point charge when $ka \to 0$.

Because the integrand in the first line of Eq. (E2) is oscillatory, it is numerically beneficial to deform the integration path in the complex s plane. Denote the integrand by $T_\sigma(s)$. The integration path is along the real line with a negative finite lower boundary, and $T_\sigma(s)$ has cuts in the complex s plane along the parts of the imaginary axis where $|s| > ka$, as shown in Fig. 14. Since $\lim_{A\to\infty} A T_\sigma(A e^{i\phi}) = 0$ in the quadrant $-\pi/2 < \phi < 0$,

$$\int_0^\infty T_\sigma(s) ds = -i \int_C T_\sigma(s) ds, \quad \text{(E5)}$$

where the contour C is shown in Fig. 14. Denoting the limit to the lower cut from the right by $s = -it + 0$, $t > ka$, expression (E3) becomes

$$R = \sqrt{(-it+0)^2 + (ka)^2} = -i\sqrt{t^2 - (ka)^2} \equiv -iR', \quad \text{(E6)}$$

while the Bessel function in Eq. (E2) may be rewritten as[68]

$$j_\sigma(-iR') = e^{-i\sigma\frac{\pi}{2}}\sqrt{\frac{\pi}{2R'}}I_{\sigma+\frac{1}{2}}(R'), \tag{E7}$$

where I denotes the modified cylindrical Bessel function of the first kind. Combining Eqs. (E5)–(E7), the integration along the positive real line in Eq. (E2) equals

$$\int_0^\infty T_\sigma(s)ds = -ie^{-i\sigma\frac{\pi}{2}}\sqrt{\frac{\pi}{2}}\int_0^\infty e^{-\frac{t}{\beta}}P_\sigma^1\left(\frac{t}{R'}\right)\frac{I_{\sigma+\frac{1}{2}}(R')}{R'^{\frac{1}{2}}}dt, \tag{E8}$$

by which the oscillatory behavior of the integrand is exchanged for exponentially damped behavior.

APPENDIX F: APPROXIMATION OF PEAK FIELD AND PULSE DURATION

The approximate electric-field spectrum, indicated in the inset of Fig. 13, has the form,

$$|E_{T\theta}(\omega)| \approx E_0\begin{cases} 1 & \omega < \omega_1 \\ \sqrt{\dfrac{\ln\omega_2 - \ln\omega}{\ln\omega_2 - \ln\omega_1}} & \omega_1 < \omega < \omega_2 \\ 0 & \omega > \omega_2 \end{cases}, \tag{F1}$$

with E_0 given by Eq. (54). According to Eq. (52) the phase of the field equals

$$\arg E_{T\theta}(\omega) = kr + \phi(\omega), \tag{F2}$$

where the term kr is equivalent to a time shift r/c in the time domain and $\phi(\omega)$ is the phase of the sum in Eq. (52). A Taylor expansion of the time-domain field $E_{T\theta}(t)$ around $t=r/c$ may now be obtained using the moments of the frequency domain field since[69]

$$\left.\frac{d^nE_{T\theta}(t)}{dt^n}\right|_{t=r/c} = e^{-in\frac{\pi}{2}}\sqrt{\frac{2}{\pi}}\mathrm{Re}\int_0^\infty \omega^n e^{i\phi(\omega)}|E_{T\theta}(\omega)|d\omega. \tag{F3}$$

Here, it has been used that $E_{T\theta}(-\omega)=E_{T\theta}^*(\omega)$ because $E_{T\theta}(t)$ is real. If $\phi(\omega)$ were zero, the field $E_{T\theta}(t)$ would be maximum at $t=r/c$, and its maximum value $E(t)_{\max}$ would simply be Eq. (F3) with $n=0$. Substituting Eq. (F1), this would yield

$$E(t)_{\max} \approx \sqrt{\frac{2}{\pi}}E_0\omega_2 \cdot \frac{\sqrt{\pi}}{2}\frac{\mathrm{erf}\left(\sqrt{\ln\frac{\omega_2}{\omega_1}}\right)}{\sqrt{\ln\frac{\omega_2}{\omega_1}}}, \quad \phi = 0. \tag{F4}$$

The first factor on the right equals the amplitude that would result if the spectrum of Fig. 13 were fully coherent up to the frequency ω_2 and zero for $\omega > \omega_2$, while the second factor corrects for the slope in the spectrum. Analysis of the actual phase of $E_{T\theta}(\omega)$ shows that it is not zero; however, it is approximately constant at $\phi \approx -\pi/4$ for all three cases. Evaluating a few more orders of Eq. (F3) and the resulting Taylor expansions of $E_{T\theta}(t)$ shows that this nonzero phase does alter the symmetry of the SPP pulse but it does not affect the maximum value of field much. Therefore Eq. (F4) is a good approximation for the maximum electric-field amplitude in the time domain.

Finally, the duration τ of the time-domain SPP pulse, which is defined by Eq. (55), is equal to

$$\tau \equiv \frac{1}{E(t)_{\max}}\int_{-\infty}^{\infty}E(t)dt = \frac{\sqrt{2\pi}E_0}{E(t)_{\max}}. \tag{F5}$$

[1] K. Wang and D. Mittleman, Nature (London) **432**, 376 (2004).
[2] T.-I. Jeon, J. Zhang, and D. Grischkowsky, Appl. Phys. Lett. **86**, 161904 (2005).
[3] Q. Cao and J. Jahns, Opt. Express **13**, 511 (2005).
[4] K. Wang and D. M. Mittleman, Phys. Rev. Lett. **96**, 157401 (2006).
[5] K. Wang and D. Mittleman, J. Opt. Soc. Am. B **22**, 2001 (2005).
[6] N. van der Valk and P. Planken, Appl. Phys. Lett. **87**, 071106 (2005).
[7] S. A. Maier, S. R. Andrews, L. Martín-Moreno, and F. J. García-Vidal, Phys. Rev. Lett. **97**, 176805 (2006).
[8] L. Shen, X. Chen, Y. Zhong, and K. Agarwal, Phys. Rev. B **77**, 075408 (2008).
[9] M. I. Stockman, Phys. Rev. Lett. **93**, 137404 (2004).
[10] J. Deibel, N. Berndsen, K. Wang, D. Mittleman, N. van der Valk, and P. Planken, Opt. Express **14**, 8772 (2006).
[11] W. Barnes, A. Dereux, and T. Ebbesen, Nature (London) **424**, 824 (2003).
[12] *Opportunities in THz Science*, report of the DOE-NSF-NIH workshop, Arlington, VA, 2004, edited by M. Sherwin, C. Schmuttenmaer, and P. Bucksbaum, available at http://www.sc.doe.gov/bes/reports/files/THz_rpt.pdf
[13] F. Keilmann, J. Microsc. **194**, 567 (1999).
[14] R. Hillenbrand and F. Keilmann, Appl. Phys. B: Lasers Opt. **73**, 239 (2001).
[15] H.-T. Chen, R. Kersting, and G. Cho, Appl. Phys. Lett. **83**, 3009 (2003).
[16] F. Buersgens, R. Kersting, and H.-T. Chen, Appl. Phys. Lett. **88**, 112115 (2006).
[17] D. Crawley, C. Longbottom, V. Wallace, B. Cole, D. Arnone, and M. Pepper, J. Biomed. Opt. **8**, 303 (2003).
[18] R. Woodward, V. Wallace, D. Arnone, E. Linfield, and M. Pepper, J. Biol. Phys. **29**, 257 (2003).
[19] K. Kneipp, Y. Wang, H. Kneipp, L. T. Perelman, I. Itzkan, R. R. Dasari, and M. S. Feld, Phys. Rev. Lett. **78**, 1667 (1997).
[20] S. Nie and S. Emory, Science **275**, 1102 (1997).
[21] R. Jacobsen, D. Mittleman, and M. Nuss, Opt. Lett. **21**, 2011 (1996).
[22] M. Walther, M. Freeman, and F. Hegmann, Appl. Phys. Lett. **87**, 261107 (2005).
[23] T.-I. Jeon and D. Grischkowsky, Appl. Phys. Lett. **85**, 6092

(2004).
[24] G. Gallot, S. Jamison, R. McGowan, and D. Grischkowsky, J. Opt. Soc. Am. B **17**, 851 (2000).
[25] R. Mendis and D. Grischkowsky, J. Appl. Phys. **88**, 4449 (2000).
[26] H. Han, H. Park, M. Cho, and J. Kim, Appl. Phys. Lett. **80**, 2634 (2002).
[27] R. Mendis and D. Grischkowsky, Opt. Lett. **26**, 846 (2001).
[28] F. Wang *et al.*, Phys. Rev. Lett. **96**, 064801 (2006).
[29] G. Carr, M. Martin, W. McKinney, K. Jordan, G. Neil, and G. Williams, Nature (London) **420**, 153 (2002).
[30] G. Carr, M. Martin, W. McKinney, K. Jordan, G. Neil, and G. Williams, J. Biol. Phys. **29**, 319 (2003).
[31] K.-L. Yeh, M. Hoffmann, J. Hebling, and K. Nelson, Appl. Phys. Lett. **90**, 171121 (2007).
[32] J. Deibel, K. Wang, M. Escarra, and D. Mittleman, Opt. Express **14**, 279 (2006).
[33] V. Ginzburg and V. Tsytovich, *Transition Radiation and Transition Scattering* (Hilger, London, 1990).
[34] V. Ginzburg and I. Frank, Zh. Eksp. Teor. Fiz. **16**, 15 (1946).
[35] M. Ter-Mikaelian, *High-Energy Electromagnetic Processes in Condensed Media* (Wiley, New York, 1972).
[36] W. Panofsky and M. Phillips, *Classical Electricity and Magnetism*, 2nd ed. (Dover, New York, 2005).
[37] A. Tremaine, J. B. Rosenzweig, S. Anderson, P. Frigola, M. Hogan, A. Murokh, C. Pellegrini, D. C. Nguyen, and R. L. Sheffield, Phys. Rev. Lett. **81**, 5816 (1998).
[38] U. Happek, A. J. Sievers, and E. B. Blum, Phys. Rev. Lett. **67**, 2962 (1991).
[39] Y. Shibata, T. Takahashi, T. Kanai, K. Ishi, M. Ikezawa, J. Ohkuma, S. Okuda, and T. Okada, Phys. Rev. E **50**, 1479 (1994).
[40] P. Kung, H.-C. Lihn, H. Wiedemann, and D. Bocek, Phys. Rev. Lett. **73**, 967 (1994).
[41] W. Op 't Root, P. Smorenburg, T. van Oudheusden, M. van der Wiel, and O. Luiten, Phys. Rev. ST Accel. Beams **10**, 012802 (2007).
[42] Y. Shen, T. Watanabe, D. A. Arena, C. C. Kao, J. B. Murphy, T. Y. Tsang, X. J. Wang, and G. L. Carr, Phys. Rev. Lett. **99**, 043901 (2007).
[43] J. van Tilborg, C. Schroeder, C. Tóth, C. Geddes, E. Esarey, and W. Leemans, Opt. Lett. **32**, 313 (2007).
[44] C. Couillaud, Nucl. Instrum. Methods Phys. Res. A **495**, 171 (2002).
[45] O. J. Luiten, S. B. van der Geer, M. J. de Loos, F. B. Kiewiet, and M. J. van der Wiel, Phys. Rev. Lett. **93**, 094802 (2004).
[46] O. Luiten, S. van der Geer, M. de Loos, F. Kiewiet, and M. van der Wiel, Proceedings of the European Particle Accelerator Conference (EPS-AG, Lucerne, 2004), p. 725.
[47] S. van der Geer, M. de Loos, T. van Oudheusden, W. O. 't Root, M. van der Wiel, and O. Luiten, Phys. Rev. ST Accel. Beams **9**, 044203 (2006).
[48] P. Musumeci, J. T. Moody, R. J. England, J. B. Rosenzweig, and T. Tran, Phys. Rev. Lett. **100**, 244801 (2008).
[49] J. Jackson, *Classical Electrodynamics*, 3rd ed. (Wiley, New York, 1998).
[50] F. Pedrotti, L. Pedrotti, and L. Pedrotti, *Introduction to Optics* (Academic, New York, 1991).
[51] P. Morse and H. Feshbach, *Methods of Theoretical Physics* (McGraw-Hill, New York, 1953).
[52] C.-T. Tai, *Dyadic Green Functions in Electromagnetic Theory* (IEEE, New York, 1993).
[53] L. Felsen, IEEE Trans. Antennas Propag. **5**, 121 (1957).
[54] K. Trott, Appl. Comput. Electromagn. Soc. J. **11**, 85 (1996).
[55] H. McDonald, *Electric Waves* (Cambridge University Press, Cambridge, England, 1902).
[56] R. Kouyoumjian, Proc. IEEE **53**, 864 (1965).
[57] K. Siegel, J. Crispin, and C. Schensted, J. Appl. Phys. **26**, 309 (1955).
[58] K. Siegel, H. Alperin, R. Bonkowski, J. W. Crispin, A. Maffett, C. Schensted, and I. Schensted, J. Appl. Phys. **26**, 297 (1955).
[59] K. Trott, P. Pathak, and F. Molinet, IEEE Trans. Antennas Propag. **38**, 1150 (1990).
[60] R. Collin and F. Zucker, *Antenna Theory* (McGraw-Hill, New York, 1969), Pt. 2.
[61] C. Walter, *Traveling Wave Antennas* (Dover, New York, 1970).
[62] M. Walther, G. Chambers, Z. Liu, M. Freeman, and F. Hegmann, J. Opt. Soc. Am. B **22**, 2357 (2005).
[63] C. J. Hirschmugl, M. Sagurton, and G. P. Williams, Phys. Rev. A **44**, 1316 (1991).
[64] O. Kellogg, *Foundations of Potential Theory* (Springer-Verlag, Berlin, 1926).
[65] I. Kapchinskii and V. Vladimirskii, Proceedings of the International Conference on High Energy Accelerators (CERN, Geneva, 1959), p. 247.
[66] J. Stratton, *Electromagnetic Theory* (McGraw-Hill, New York, 1941).
[67] I. Gradshteyn and I. Ryzhik, *Table of Integrals, Series, and Products*, 7th ed. (Elsevier, New York, 2007).
[68] M. Abramowitz and I. Stegun, *Hankbook of Mathematical Functions* (Dover, New York, 1972).
[69] A. Papoulis, *The Fourier Integral and Its Applications* (McGraw-Hill, New York, 1962).